Density-Functional-Theory Modeling of Cation Diffusion in Bulk $La_{1-x}Sr_xMnO_{3\pm\delta}$ ($x = 0.0$–0.25) for Solid-Oxide Fuel-Cell Cathodes

Yueh-Lin Lee,[1,*] Yuhua Duan,[1,†] Dane Morgan,[1,2] Dan C. Sorescu,[1] Harry Abernathy,[3,4] and Gregory Hackett[1,3]

[1]*National Energy Technology Laboratory, United States Department of Energy, 626 Cochrans Mill Road, P.O. Box 10940, Pittsburgh, Pennsylvania 15236-0940, USA*

[2]*Department of Materials Science and Engineering, University of Wisconsin-Madison, Madison, Wisconsin 53706, USA*

[3]*National Energy Technology Laboratory, United States Department of Energy, 3610 Collins Ferry Road, P.O. Box 880, Morgantown, West Virginia 26507-0880, USA*

[4]*AECOM, Morgantown, West Virginia 26507-0880, USA*

(Received 11 March 2017; revised manuscript received 19 July 2017; published 4 October 2017)

In this work, the A- and B-site cation migration pathways involving defect complexes in bulk $La_{1-x}Sr_xMnO_{3\pm\delta}$ (LSM) at $x = 0.0$–0.25 are investigated based on density-functional-theory modeling for solid-oxide fuel-cell (SOFC) cathode applications. We propose a dominant A-site cation migration mechanism which involves an A-site cation (e.g., La_A^x) hop into a V_A''' of a V_A'''-V_B''' cluster, where La_A^x, V_A''', and, V_B''' are La^{3+}, A-site vacancy, and B-site vacancy in bulk LSM, respectively, and V_A'''-V_B''' is the first nearest-neighbor V_A''' and V_B''' pair. This hop exhibits an approximately 1.6-eV migration barrier as compared to approximately 2.9 eV of the La_A^x hop into a V_A'''. This decrease in the cation migration barrier is attributed to the presence of the V_B''' relieving the electrostatic repulsion and steric constraints to the migrating A-site cations in the transition-state image configurations. The V_A'''-V_B''' interaction energy is predicted to be weakly repulsive (0.2–0.3 eV) in bulk LSM, which enables the V_A'''-V_B''' cluster to readily form. The predicted apparent activation energy of D_{La}^* in $LaMnO_{3\pm\delta}$ (LMO) for the A-site migration pathway is about 1.4 eV, in good agreement with the experimental A-site cation impurity diffusivity measurements. By examining the A-site cation migration barriers among different metal cations (Zr^{4+}, Y^{3+}, Gd^{3+}) relevant for SOFC applications, it is demonstrated that migration barriers of the cation impurity in bulk LSM correlate with the ionic charge and ionic radius at a given formal cationic charge. The B-site cation migration barrier takes place by an analogous mechanism that involves a Mn_B^x (Mn^{3+} on the B site) hop into a V_B''' *via* the Mn_B^x-$V_A''' \rightarrow V_B'''$ path with the same cation transport carrier of V_A'''-V_B'''. This diffusion pathway is found to have a barrier of approximately 1.6 eV, similar to the analogous A-site hop. However, hopping of the Mn_A^x antisite defect (Mn^{3+} on the A site) to a nearest-neighbor V_A''' [Mn_A^x (V_A''') mechanism] has a barrier of only 0.5 eV. Such a low Mn_A^x (V_A''') migration barrier opens the possibility to activate Mn transport in bulk LSM through the diffusion of the antisite Mn_A^x (V_A''') pathway on the A-site lattice, particularly when the concentration of the Mn antisite defect can be altered upon varying the A/B ratio and the activity of MnO_y. The increase in Sr_A' doping concentration in bulk $La_{1-x}Sr_xMnO_{3\pm\delta}$ ($x = 0.0$–0.25) is found to influence primarily the formation energies of cation transport carriers (cation vacancies), whereas the cation migration barriers exhibit only a weak dependence on the Sr_A' concentration.

DOI: 10.1103/PhysRevApplied.8.044001

I. INTRODUCTION

Solid-oxide fuel cells (SOFCs) are alternative energy and power-generation sources with significant advantages of being highly efficient, fuel flexible, modular, and scalable. After several decades of research and development, SOFCs are beginning to be commercialized as reliable backup power systems and as combined power and hot water systems for residential usage. Producing systems that can perform reliably for more than 50 000 h, enhancing the cell performance, and decreasing the long-term performance degradation rate are some of the major research and development goals in the SOFC program at the National Energy Technology Laboratory [1].

Understanding the factors governing compositional and microstructural changes in cathode materials and their interfaces with electrolytes during operation is a critical aspect of SOFC performances and their long-term stability, since changes in the surface and interfacial compositions and microstructures strongly influence the available surface area and the active triple-phase boundaries necessary for

*Corresponding author.
Yueh-Lin.Lee@netl.doe.gov
†Corresponding author.
Yuhua.Duan@netl.doe.gov

oxygen reduction [2,3]. In particular, for the state-of-the-art $La_{1-x}Sr_xMnO_{3\pm\delta}$ (LSM) SOFC cathode materials, cation transport plays a critical role in controlling reaction kinetics of the secondary-phase formation [4,5], segregation and changes in surface composition [6], grain growth or sintering [7–10], creep deformation [11,12], and in the creation of diffuse interfaces between cell components [13,14]. Despite many phenomenological observations of microstructure and compositional evolution of LSM cathodes and their interfaces with electrolytes that are directly or indirectly associated with cation transport, fundamental mechanistic understanding is still insufficient to fully describe the experimental cation diffusivities including their dependences on temperature (T), partial pressure of oxygen (pO_2), and applied potentials, in both bulk LSM and its interfaces under SOFC operating conditions [13,15–17]. Several experimental studies have reported the LSM and $LaMnO_{3\pm\delta}$ (LMO) bulk cation diffusivities and their temperature dependences [13,15–17] and differences ranging between 1.5 and 2 eV in the apparent activation energies for the cation diffusivities, were found among different experimental methods used (e.g., solid-state reaction versus tracer diffusion and interdiffusion of diffusion couples). In addition, Sr substitution of about 20–30 at. % is generally introduced at the A site of LMO as cathode materials for SOFCs in order to promote electronic conductivity, to enhance the oxygen reduction activity, and to increase chemical and mechanical stability with yittria-stabilized-zirconia (YSZ) electrolytes [18,19]. However, limited experimental cation diffusivities can be found in the literature for Sr-substituted LMO [13], and it remains unclear how cation diffusivities in LSM and their temperature dependences couple to the Sr substitution level.

Because of the close-packed nature of the perovskite lattice, which electrostatically and sterically hinders formation of cation interstitials, the cation diffusion in crystalline LSM primarily takes place *via* cation-vacancy mediated diffusion mechanisms [15–17,20]. Since nonstoichiometry and defect concentration (for both cation and anion vacancies) can be substantial in bulk LSM, understanding of the LSM bulk defect chemistry is critical to systematic interpretation of the experimental cation tracer diffusivity results [15,17,20,21]. Specifically, the cation-vacancy concentration is up to 1%–5% in LMO and LSM in air under the typical SOFC operating temperatures [15,17,20–22], a fact that can facilitate long-range cation diffusion. Based on the experimental oxygen nonstoichiometry measurements and by solving a system of coupled nonlinear equations associated with metal conservation, lattice site balance, charge neutrality, and equilibrium constants of the major defect reactions, detailed information on point-defect concentrations in LSM bulk versus T and pO_2 can be systematically modeled [23–27]. *Ab initio*–based defect-formation energies, defect interaction energies, and entropies can be further used to verify the model assumptions associated with the key defect reactions in LSM, thereby reducing the defect model uncertainty and yielding insight into defect interactions in bulk LSM [27].

In addition to the carrier concentrations for cation transport, activation barriers of cation migration also have to be determined to predict the rates of the cation diffusion. While several possible cation diffusion pathways have been proposed in the previous studies, including transport of cation-vacancy complexes in bulk LMO and LSM [15,17,20,21,28,29] or related SOFC perovskites such as $La_{1-x}Sr_xGa_{1-y}Mg_yO_{3-(x+y)/2}$ [30,31], only few theoretical studies were performed to date to simulate the cation migration barriers [20,29,30]. Energy differences of approximately 1 eV were found among the simulated A-site cation migration barriers mediated by an A-site vacancy in bulk LMO between the empirical potentials method as described in Ref. [20] versus the density-functional-theory (DFT) results in Ref. [29]. By incorporating the calculated migration barriers from the two studies in conjunction with kinetic Monte Carlo (KMC) simulations [29], it was further shown that significant differences in the magnitude of the predicted A-site cation diffusivities exist [29]. Nonetheless, in the absence of the experimental results specific to the simulated LSM compositions ($x = 0.2$–0.3), the accuracy of the corresponding computed migration energies provided in Refs. [20,29] cannot be verified. Furthermore, both the simulated A-site cation migration barriers obtained using DFT modeling [29] and empirical potentials [20] are still at least 1–2 eV higher than the experimentally extracted apparent activation energies for Pr impurities on A sites in LMO [32], which suggests that there may exist alternative lower-barrier cation migration pathways.

As with A-site diffusion, the understanding of the B-site diffusion mechanisms in LSM is still quite poor. For example, an active Mn cation diffusion pathway was suggested to involve a B-site metal hopping *via* an A-site-and-B-site vacancy cluster [16,21,28], but concentration of the A-site-and-B-site vacancy clusters in LSM is not directly available from solving the LSM bulk point-defect models, and, consequently, it is difficult to assess the predictive ability of this diffusion model. An energy difference of approximately 2.2 eV was found by Miyoshi and Martin [16] by comparing the experimental apparent activation energies of the Mn tracer diffusivities in LMO with the reported migration barriers determined based on empirical potential simulations [20] and by taking into account the estimated effective formation enthalpy of the cation vacancies based on experimental oxygen nonstoichiometry measurements [23]. Miyoshi and Martin [16] hypothesized that the 2.2 eV difference could be compensated by a −2.2 eV attraction between an A-site vacancy and a B-site vacancy, but they also pointed out that justification of such a strong attraction interaction needed additional theoretical simulations or experimental measurements for validation.

In this work, the cation transport mechanisms and their migration barriers in bulk $La_{1-x}Sr_xMnO_{3\pm\delta}$ at $x = 0.0$–0.25 under the SOFC operating conditions are investigated based on the density-functional theory (DFT). Combining with the bulk LSM defect modeling, the cation diffusion coefficients are assessed from both the concentration of the transport carriers, including concentration of relevant defect clusters and their temperature dependences, as well as the migration barriers associated with the *A*-site and *B*-site cation transport in bulk LSM. The main goal of this study is to employ first-principles DFT calculations to determine the cation transport mechanisms with a goal of resolving the existing discrepancies between the theoretical modeling and the available experimental LSM cation diffusivities, as well as to identify how such a diffusion might be manipulated to improve LSM SOFC cathode stability. This work is organized as follows: Sec. II describes the computational modeling approaches used in this study. Section III discusses the $La_{1-x}Sr_xMnO_{3\pm\delta}$ bulk defect modeling and the defect interactions used to extract transport carrier concentration *versus* T and pO_2. Section IV summarizes the theoretical results of the investigated cation migration mechanisms and the corresponding barriers in bulk LSM. Section V discusses the T dependences of the cation tracer diffusion coefficients in bulk LSM at $x = 0.0$ and 0.3 based on a three-dimensional random-walk diffusion model, and Sec. VI contains the summary and conclusions of this work.

II. COMPUTATIONAL MODELING APPROACHES

A. Density-functional-theory modeling methods

Spin-polarized DFT calculations are performed with the Vienna *ab initio* simulation package [33,34] (VASP) using the projector-augmented plane-wave (PAW) method [35]. Exchange correlation is treated using the Perdew-Burke-Ernzerhof [36] (PBE) generalized-gradient approximation (GGA). The GGA + U calculations [37] are performed with the simplified spherically averaged approach [38], where the U_{eff} (U_{eff} = Coulomb U − exchange J) is applied to the d electrons of Mn with $U_{\text{eff}}(\text{Mn}) = 4.0$ eV [27,39,40].

The electronic configurations of the species and their names in the VASP-supplied PAW potentials are La ($5s2\,5p6\,6s2\,5d1$), Sr ($4s2\,4p6\,5s2$), Mn_{pv} ($3p6\,3d6\,4s1$), and O (normal oxygen) ($2s2\,2p4$). The plane-wave energy cutoff is 600 eV, and a Monkhorst-Pack [41] k-point mesh equivalent to $8 \times 8 \times 8$ for the primitive perovskite unit cell is used to sample the Brillouin zone.

An orthorhombic supercell ($\boldsymbol{a}_{\text{supercell}} = \boldsymbol{a}_{\text{orthorhombic}} - \boldsymbol{b}_{\text{orthorhombic}}$, $\boldsymbol{b}_{\text{supercell}} = \boldsymbol{a}_{\text{orthorhombic}} + \boldsymbol{b}_{\text{orthorhombic}}$, $\boldsymbol{c}_{\text{supercell}} = \boldsymbol{c}_{\text{orthorhombic}}$, where $\boldsymbol{a}_{\text{orthorhombic}}$, $\boldsymbol{b}_{\text{orthorhombic}}$, and $\boldsymbol{c}_{\text{orthorhombic}}$ are the lattice vectors of the experimental orthorhombic LSM [42]) is first constructed based on the experimental symmetry [42] and then fully relaxed in the ferromagnetic state in the DFT simulations. The lattice constants of the 40-atom supercell are then set to be equal to the cube root of the relaxed volume and then by performing iterations between the internal relaxation and volume relaxation (with fixed atomic coordinate and shape). This approach allows us to maintain the BO_6 octahedral rotation in the supercell during ionic relaxation while maintaining a cubic shape [27,40]. The constructed supercells are analogous to a $2\boldsymbol{a}_{\text{cubic}} \times 2\boldsymbol{a}_{\text{cubic}} \times 2\boldsymbol{a}_{\text{cubic}}$ cubic perovskite supercell ($\boldsymbol{a}_{\text{cubic}}$ is the lattice constant of the cubic perovskite). These settings are used to approximate the geometric characteristics of the conductive cubic paramagnetic phases of LMO and LSM that occur at typical SOFC operating temperatures (600–800 °C) and provide a consistent and tractable set of magnetic structures [27,40]. Larger supercells are further constructed based on the $2\boldsymbol{a}_{\text{cubic}} \times 2\boldsymbol{a}_{\text{cubic}} \times 2\boldsymbol{a}_{\text{cubic}}$ pseudocubic perovskite supercell, including a 80-atom $2\sqrt{2}\boldsymbol{a}_{\text{cubic}} \times 2\sqrt{2}\boldsymbol{a}_{\text{cubic}} \times 2\boldsymbol{a}_{\text{cubic}}$, an 160-atom $2\sqrt{2}\boldsymbol{a}_{\text{cubic}} \times 2\sqrt{2}\boldsymbol{a}_{\text{cubic}} \times 4\boldsymbol{a}_{\text{cubic}}$, and a 320-atom $4\boldsymbol{a}_{\text{cubic}} \times 4\boldsymbol{a}_{\text{cubic}} \times 4\boldsymbol{a}_{\text{cubic}}$ supercell for defect-formation and cation migration barrier calculations. For the defect calculations, relaxation of the atomic positions is conducted until Hellmann-Feynman forces are below 1 meV Å^{-1}. All the LMO and LSM defect calculations in this work are performed using neutral supercells (without manual adjustment of the charge in the supercell), and, therefore, the introduced defect charge in the supercell is automatically accommodated. Cation migration energies are simulated using the climbing-image nudged-elastic-band method (CINEB) at $x = 0.25$ with at least three images per calculation [43].

For LSM, the Sr'_A dopant (Sr^{2+} dopant in an *A*-site lattice based on the Kröger-Vink notation [44]; the symbols of the ionic and defect species in bulk LSM adopted in this work are summarized in Table S1 of the Supplemental Material [45]) is introduced in the simulated supercells at the concentration $x = 0.25$ for calculating the defect energetics and cation migration energies. Considering the repulsive interaction between Sr'_A dopants, a Sr'_A ordering with the farthest separation of all the Sr'_A dopants in the simulated supercells is used in the defect and migration barrier calculations (as shown in Fig. S1 of Ref. [45]). Two additional Sr configurations are investigated to compare the energetic differences among different Sr configurations (Fig. S1 of Ref. [45]). Our results indicate that the dependences of the cation migration barriers on the Sr configuration in bulk $La_{0.75}Sr_{0.25}MnO_3$ are weak, as the migration barrier differences among the three Sr arrangements in bulk LSM are within 0.1 eV for the active La and Mn migration pathways, as shown in Fig. S2 of Ref. [45]. The effect of the magnetic ordering on cation migration barriers of the energetically most favorable pathways is also examined. Comparing the results of the ferromagnetic and the stable *A*-type antiferromagnetic calculations, we find that the differences in the barriers are approximately 0.1 eV,

as shown in Fig. S3 of Ref. [45]. This relatively small change between ferromagnetic and stable antiferromagnetic structures suggests that the migration barriers are weakly affected only by the magnetic state, supporting our use of a simple ferromagnetic structure in place of the disordered paramagnetic structure. While the *G*-type antiferromagnetic ordering was previously adopted to simulate the oxygen-vacancy formation energies versus Sr concentration in LMO (between $x = 0$ and $x = 0.5$), in the case of high temperatures in the paramagnetic state [46], this particular *G*-type antiferromagnetic state has been shown to be an energetically unfavorable state in LMO using both the PBE and hybrid functional calculations as compared to the *A*-type and *C*-type antiferromagnetic ordering [47] and is, therefore, not included in our DFT cation migration simulation.

The calculated migration barriers exhibit a weak energy dependence on the supercell sizes (i.e., defect concentration; see Table S2 of Ref. [45]), with a difference of approximately 0.3 eV or less between the 80-atom, 160-atom, and 320-atom supercells. This range of the approximately 0.3-eV barrier variation contains at least two types of defect concentration effects among different supercell sizes: (i) nondilute cation-vacancy concentration in bulk LSM at thermodynamic equilibrium for calculating the migration barriers; considering the high cation-vacancy concentration in LSM at $x = 0.0$–0.25 in air under SOFC operating temperature [23], it is desirable to use the supercell size with cation-vacancy concentration close to equilibrated oxygen overstoichiometry. (ii) The self-interaction of the migrating cations in the finite-size supercell where there is spurious defect interaction. The self-interaction term is considered to be a weaker contribution based on the first-order correction term for the electrostatic interaction in the finite-size supercell [48] due to moderately high dielectric properties under the SOFC conditions [49]. Although the supercell size dependences of the defect energetics and the migration barriers can be further performed to extrapolate to a dilute limit, a thorough investigation requires significant computation time and makes the complex studies being developed here impractical. Therefore, in this work, the cation migration barriers used for calculating cation diffusion coefficients are based on the results simulated with the $2\sqrt{2}\boldsymbol{a}_{\text{cubic}} \times 2\sqrt{2}\boldsymbol{a}_{\text{cubic}} \times 2\boldsymbol{a}_{\text{cubic}}$ and $2\sqrt{2}\boldsymbol{a}_{\text{cubic}} \times 2\sqrt{2}\boldsymbol{a}_{\text{cubic}} \times 4\boldsymbol{a}_{\text{cubic}}$ pseudocubic supercells, as shown in Fig. S4(a) of Ref. [45]. These cell sizes likely produce errors of about 0.2 eV in the calculated barriers due to the finite-size effects based on the weak dependences to the Sr disorder configurations and supercell sizes.

B. $La_{1-x}Sr_xMnO_{3\pm\delta}$ bulk defect modeling

To calculate the concentration of transport carriers for cation diffusion in bulk LSM at $x = 0$ and 0.2, we first solve the $La_{1-x}Sr_xMnO_{3\pm\delta}$ bulk defect model by combining the defect energetics simulated with *ab initio* modeling [27] and the defect-formation entropies (estimated based on empirical thermodynamic free-energy and entropy data of the O_2 gas phase and a simple Einstein model for the exchanged O^{2-} ions in the solid phase) [40]. The experimental $LaMnO_{3\pm\delta}$ and $La_{0.8}Sr_{0.2}MnO_{3\pm\delta}$ oxygen nonstoichiometry versus pO_2 and T data measured by thermogravimetry analysis [23,50] are then used to serve as empirical constraints for adjustment and validation of the *ab initio*–based defect model parameters. Table I summarizes the defect-formation energies, defect-concentration-dependent nonideal terms, and defect-formation entropies used in the defect modeling. Details of the LSM bulk defect modeling approach used in this work are described in Ref. [27] and in Sec. S1 of Ref. [45]. An additional artificial constraint requiring an equal amount of $[V_A'''']$ and $[V_B'''']$ in

TABLE I. The main defect reactions and parameters used in the *ab initio*–and empirical-based bulk defect models for $LaMnO_{3\pm\delta}$ [27] and $La_{0.8}Sr_{0.2}MnO_{3\pm\delta}$. The interaction energy parameter in the unit of electron volts per defect is defined as change of the defect-formation reaction energy as a function of defect concentration of $V_O^{\bullet\bullet}$ (for oxygen-vacancy formation) and a separated V_A''' and V_B''' pair (for cation-vacancy formation) in $LaMnO_{3\pm\delta}$ [27] and $La_{0.8}Sr_{0.2}MnO_{3\pm\delta}$.

	$LaMnO_{3\pm\delta}$ [27]			$La_{0.8}Sr_{0.2}MnO_{3\pm\delta}$		
Defect-formation reaction	$\Delta E_{\text{reaction}}$ (eV)	Interaction (eV per defect)	Defect-reaction entropy, $\Delta S_{\text{reaction}}$ [a] (meV/K)	$\Delta E_{\text{reaction}}$ (eV)	Interaction (eV per defect)	Defect-reaction entropy, $\Delta S_{\text{reaction}}$ (meV/K)
Oxygen-vacancy formation $2Mn_B^x + O_O^x \rightarrow 2Mn_B' + V_O^{\bullet\bullet} + \frac{1}{2}O_2^{\text{gas}}$	3.56	2.54	$-\Delta S_{\text{reaction}}$ [a]	2.91	1.2	$-\Delta S_{\text{reaction}}$ [a]
Cation-vacancy formation $6Mn_B^x + \frac{3}{2}O_2^{\text{gas}} \rightarrow 6Mn_B^{\bullet} + V_A'''' + V_B'''' + 3O_O^x$	−4.07	16.10	$3\Delta S_{\text{reaction}}$ [a]	−3.92	59.2	$3\Delta S_{\text{reaction}}$ [a]
Charge disproportionation $2Mn_B^x \rightarrow Mn_B^{\bullet} + Mn_B'$	0.06	0	0	0.00	0	0

[a] $\Delta S_{\text{reaction}} = [(4.552 \times 10^{-5})(T - 0.894)]$ (meV/K) for the reaction of O^{2-} (solid)$\rightarrow 1/2 \bullet O^2$(gas) $+ 2e^-$ obtained from a linear fit of the $\Delta S_{\text{reaction}}$ versus T plot, e.g., Fig. 2 of Ref. [27].

bulk LMO and LSM is also imposed in this defect model, which is based on the nominal A/B ratio of the LMO and LSM samples used in the experimental measurements [23,50]. It is also noted that in the discussions below, the DFT defect interaction energies of the bulk LSM simulated at $x = 0.25$ are directly used to calculate the defect cluster concentrations at $x = 0.2$ based on the bulk defect model that is fit with the experimental oxygen nonstoichiometry, as shown in Fig. S5 of Ref. [45]. Similarly, the cation migration barrier calculations simulated at $x = 0.25$ are directly used in combination with the bulk defect model for assessing the T dependences of the cation diffusivities at $x = 0.2$.

C. Simple random-walk assessment of the cation self-diffusion coefficients

The relevant point and cluster defect concentrations and the cation migration barriers of the possible diffusion pathways obtained using the methods that we describe above are further incorporated into a three-dimensional random-walk diffusion formalism to assess the terms in an Arrhenius expression for the cation diffusion coefficients in bulk $La_{1-x}Sr_xMnO_{3\pm\delta}$ ($x = 0.0$ and 0.2). Further optimization is then performed by fitting the Arrhenius expression prefactor, which is due to factors such as the migration entropy and the attempt frequency, to the experimental cation diffusivities. The generalized form of the cation tracer diffusion coefficients based on the three-dimensional random-walk formalism can be described as the following [51]:

$$D^*_{\mathrm{cat}} = \left(A\frac{Z}{6}d^2\right)[\mathrm{def}(T, pO_2)]\exp\left(-\frac{\Delta E_{\mathrm{mig}}}{k_B T}\right), \quad (1)$$

where $[\mathrm{def}(T, pO_2)]$ is the concentration of defect carriers as a function of T and pO_2 for cation diffusion, Z is the number of neighboring sites to which the defect can migrate, d is the jump distance (e.g., lattice constant of LSM perovskites), ΔE_{mig} and ΔS_{mig} are the energy and entropy of migration, k_B is the Boltzmann constant, and T is the temperature. The first bracket in Eq. (1) is a constant $A = f^*\nu_0\exp[(\Delta S_{\mathrm{mig}})/k_B]$, where f^* is the correlation factor, and ν_0 is the attempt frequency, are fit to experimental cation diffusivities. More details of the diffusion coefficient formalism are provided in Sec. S2 of Ref. [45]. It is noted that for a cluster mechanism, the correlation factor f^* can become a function of the individual defect jump frequencies and the defect concentrations [51]. In principle, the tracer correlation factors can be assessed by Monte Carlo simulations or analytic solutions with given jump frequencies and paths of the species. For example, Belova *et al.* [52] performed such an analysis on the $La_{1-x}Sr_xGa_{1-y}Mg_yO_{3-(x+y)/2}$ perovskite and obtained the tracer correlation factor ratio as a function of the exchange frequency ratio for the vacancy cluster diffusion mechanisms proposed by Schultz *et al.*[31]. However, since the identified active cation diffusion pathways in LMO and LSM in this study are different from the cluster diffusion mechanisms in the LSGM perovskite oxides (as we discuss in Sec. IV), such an analysis has to be performed additionally for LMO and LSM based on the energy landscapes of the possible cation diffusion pathways. In the first approximation, this study assumes that the tracer correlation factors exhibit no or weak temperature dependences in the temperature regime where the experimental cation diffusivity measurements are performed. Consequently, the temperature dependences in the calculated cation tracer diffusion coefficients following Eq. (1) mainly come from the defect energetics of the transport carriers and the associated migration barriers of the cation migration mechanisms.

III. $La_{1-x}Sr_xMnO_{3\pm\delta}$ BULK DEFECT CHEMISTRY AND DEFECT INTERACTIONS

A. Point-defect concentration in bulk $La_{1-x}Sr_xMnO_{3\pm\delta}$ versus T and pO_2

The point-defect concentrations $[Mn_B^x]$, $[Mn_B^\bullet]$, $[Mn_B']$, $[V_A'''']$, $[V_B'''']$, and $[V_O^{\bullet\bullet}]$ are indicated using Kröger-Vink notation (a description of the symbols used in this work is summarized in Table S1 of Ref. [45]) *versus* pO_2 at $T = 1073$, 1273, and 1473 K can be extracted by solving the $LaMnO_{3\pm\delta}$ and $La_{0.8}Sr_{0.2}MnO_{3\pm\delta}$ bulk defect model and are provided in the Brouwer diagrams [53] of Fig. 1. The model predicted versus the experimental oxygen nonstoichiometry results are shown in Fig. S5 of Ref. [45]. Again, it is noted that an artificial constraint corresponding to an equal amount of $[V_A'''']$ and $[V_B'''']$ in bulk LMO and LSM is imposed in the defect model. The influence of varying the A/B ratio of LSM on the bulk oxygen nonstoichiometry or defect chemistry [54,55] and ionic diffusivities [7,18] remains an open topic of interest for further theoretical modeling and experimental measurements. In Sec. III B, the extracted LSM bulk point-defect concentration at the A/B ratio equal to 1 under SOFC operating conditions is utilized to assess the carrier concentration of the defect complexes that are involved in the cation transport mechanisms based on the calculated defect interaction energies.

B. Defect interactions and concentration of defect clusters

For the investigated cation diffusion mechanisms (as we discuss in more detail in Sec. IV), the defect complexes of V_A''''-V_B'''', $V_O^{\bullet\bullet}$-V_A'''', $V_O^{\bullet\bullet}$-V_B'''', and $V_O^{\bullet\bullet}$-V_A''''-V_B'''' are involved as the cation transport vehicles. To assess the LSM cation diffusion coefficients of these cation transport mechanisms, it is important to calculate the concentration of the defect complexes as a function of T to separate the contributions of the associated defect energetics from the migration

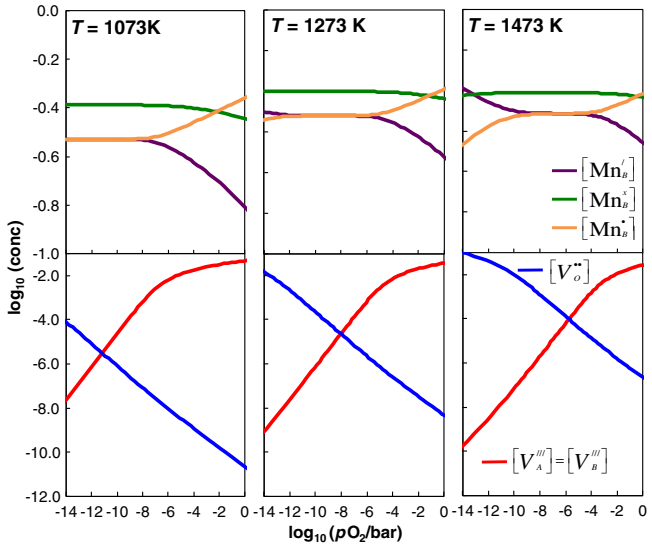

(a) $LaMnO_{3\pm\delta}$

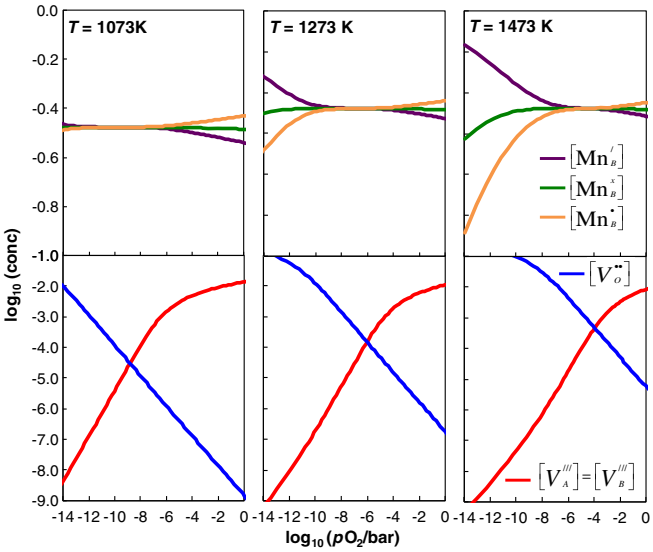

(b) $La_{0.8}Sr_{0.2}MnO_{3\pm\delta}$

FIG. 1 The predicted point-defect concentrations (conc) ($[Mn_B^x]$, $[Mn_B^\bullet]$, $[Mn_B']$, $[V_A'''']$, $[V_B'''']$, and $[V_O^{\bullet\bullet}]$) versus pO_2 at $T = 1073$, 1273, and 1473 K in (a) $LaMnO_{3\pm\delta}$ and (b) $La_{0.8}Sr_{0.2}MnO_{3\pm\delta}$ in the Brouwer diagram. The results are based on fittings to the experimental nonstoichiometry data of LSM [23,50].

barriers. For practical considerations [27], the concentrations of the defect complexes are calculated directly through the defect association reactions using the defect interaction energies obtained from DFT simulations (as we detail below), whereas other terms such as configurational and vibrational entropy are neglected. We note that even if such an approximation can introduce certain errors through neglecting the configurational entropy terms (estimated to be approximately 1 order of magnitude in concentration of the species) in the predicted defect cluster concentration, the main focus of this work is on the mechanistic information of the cation migration, which is less sensitive to the errors introduced in the absolute quantities of the cation diffusivities.

Taking the reaction to form a V_A''''-V_B'''' defect complex as an example, a defect association reaction can be written as

$$V_A'''' + V_B'''' \rightarrow V_A'''' - V_B'''', \tag{2}$$

where the equilibrium constant of the defect association reaction can be calculated as

$$K_{\text{association}} = \exp\left(-\frac{\Delta E_{\text{association}}}{k_B T}\right) = \frac{[V_A'''' - V_B'''']}{[V_A''''][V_B'''']}. \tag{3}$$

$\Delta E_{\text{association}}$ is obtained from total energy differences between a $4\boldsymbol{a}_{\text{cubic}} \times 4\boldsymbol{a}_{\text{cubic}} \times 4\boldsymbol{a}_{\text{cubic}}$ perovskite supercell with a first nearest-neighbor $V_A'''' - V_B''''$ defect pair versus that with the farthest-neighbor defect pair in the DFT simulations. More details of the defect configurations and defect interaction energy calculations are provided in Fig. S4 of Ref. [45]. Therefore, the concentration of the defect complex $[V_A''''$-$V_B'''']$ in $La_{1-x}Sr_xMnO_{3\pm\delta}$ can be calculated as

$$[V_A'''' - V_B''''] = [V_A''''][V_B''''] \exp\left(\frac{-\Delta E_{\text{association}}}{k_B T}\right), \tag{4}$$

where $[V_A'''']$ and $[V_B'''']$ can be obtained from the bulk defect model (Fig. 1). It is noted that Eq. (4) implicitly assumes $[V_A''''$-$V_B''''] \ll [V_A''''](= [V_B''''])$, and before calculating, the corresponding association (interaction) energy $[V_A''''$-$V_B'''']$ cannot be known. The obtained $[V_A''''$-$V_B'''']$ from Eq. (4) is further used to calculate the concentration of $[V_O^{\bullet\bullet}$-$(V_A''''$-$V_B'''')]$ following the same derivation as described above and using the calculated DFT interaction energies from a first nearest-neighbor $V_O^{\bullet\bullet}$-$(V_A''''$-$V_B'''')$ relative to the separate V_A''''-V_B'''' and $V_O^{\bullet\bullet}$ systems in a $4\boldsymbol{a}_{\text{cubic}} \times 4\boldsymbol{a}_{\text{cubic}} \times 4\boldsymbol{a}_{\text{cubic}}$ pseudocubic supercell. For Sr_A' diffusion, the Sr_A'-V_A'''' defect cluster is also regarded as the transport carrier, and the Sr_A'-V_A'''' interaction is estimated to be +0.2 eV based on the Sr_A'-V_A'''' interaction energy versus the pair distance profile reported in Ref. [29] and by assuming the second nearest-neighbor Sr_A'-V_A'''' pair (approximately 5.6 A) is the stable configuration in LSM.

Table II summarizes the calculated DFT defect interaction energies of V_A''''-V_B'''', V_B''''-$V_O^{\bullet\bullet}$, V_A''''-$V_O^{\bullet\bullet}$, V_A''''-V_B''''-$V_O^{\bullet\bullet}$, and Sr_A'-V_A'''' in bulk $La_{1-x}Sr_xMnO_3$ at $x = 0.0$ and 0.25. The defect interaction energies are calculated by taking the total energy difference of the nearest-neighbor defect pair versus the separated defect pair (at least 8 Å) in a 320-atom LSM bulk supercell, with sampling of three or more defect pairs for each defect-pair type on different lattice sites. A range of the calculated defect interaction energies is provided in Table II based on the sampled configurations, which considers the range of the calculated defect

TABLE II. Summary of the calculated DFT defect interaction energies of V_A'''-V_B''', $V_O^{\bullet\bullet}$-V_A''', $V_O^{\bullet\bullet}$-V_B''', $V_O^{\bullet\bullet}$-$(V_A'''$-$V_B''')$, and Sr_A'-V_A''' in bulk $La_{1-x}Sr_xMnO_{3\pm\delta}$ ($x = 0.0$ and 0.2) within $4\boldsymbol{a}_{\text{cubic}} \times 4\boldsymbol{a}_{\text{cubic}} \times 4\boldsymbol{a}_{\text{cubic}}$ pseudocubic supercells. A range of the calculated defect interaction energies is provided in this table based on the sampled configurations.

	$x = 0.0$	$x = 0.25$
V_A'''-V_B'''	+(0.2 − 0.3) eV	+(0.2–0.3) eV
$V_O^{\bullet\bullet}$-V_A'''	−(1.1–1.3) eV	−(0.5–0.7) eV
$V_O^{\bullet\bullet}$-V_B'''	−(0.8–1.0) eV	−(0.6–0.8) eV
$V_O^{\bullet\bullet}$-$(V_A'''$-$V_B''')$	−(0.7–1.0) eV	+(1.0–1.2) eV
Sr_A'-V_A'''	⋯	+0.2 eV (Ref. [29])

interaction energies among the sampled defect configurations. More details of the defect configurations used to calculate the defect interactions are provided in Fig. S4(b) of Ref. [45]. We note that the defect interaction energy assessment performed here is mainly to evaluate the relative energy scale of the defect interactions for the different types of defect clusters involved in the cation transport. Lattice Monte Carlo simulations based on the cluster expansion approach can be further performed to obtain more detailed descriptions of the potential energy profiles [56].

Figure 2 shows the calculated concentration of the defect complex, V_A'''-V_B''', V_A'''-$V_O^{\bullet\bullet}$, V_B'''-$V_O^{\bullet\bullet}$, and V_A'''-V_B'''-$V_O^{\bullet\bullet}$ versus $1/T$ ($T = 1073$–1473 K) at $pO_2 = 0.2$ atm for $La_{1-x}Sr_xMnO_{3\pm\delta}$ at $x = 0.0$ and 0.2 based on the point-defect concentration extracted from the bulk LSM defect model and the defect interaction energies in Table I. The effective formation energies of the defect complexes are also extracted from the slopes of log concentration versus $1/T$. These results suggest the following:

(a) Weak repulsive interaction energies exist between $\boldsymbol{V_A'''}$ and $\boldsymbol{V_B'''}$. The slopes of log $[V_A''']$ (or $[V_B''']$) versus $1/T$ suggest slightly negative effective formation energies, which can be explained by the oxygen overstoichiometry versus $1/T$ of LSM at $x = 0.0$ and 0.2 in the temperature range of 1073–1473 K in air (the cation-vacancy content can be calculated based on the oxygen overstoichiometry). More specifically, since the calculated V_A'''-V_B''' interaction energies are +0.34 eV at $x = 0.0$ and +0.17 eV at $x = 0.25$, they have a relatively weak repulsive interaction compared to their overall formation energies, so the temperature dependences of $[V_A'''$-$V_B''']$ are close to $[V_A'''][V_B''']$ [Eq. (4)].

(b) Moderate attractive interaction energies for the $V_O^{\bullet\bullet}$-V_A''', $V_O^{\bullet\bullet}$-V_B''', and $V_O^{\bullet\bullet}$-$(V_A'''$-$V_B''')$ defect clusters. The DFT simulations suggest there is a moderate attractive interaction (0.5–1.3 eV) between $V_O^{\bullet\bullet}$ and V_A''', V_B''', as well as the $V_O^{\bullet\bullet}$-$(V_A'''$-$V_B''')$ cluster in bulk LSM, in comparison with the weak repulsive interaction energy between V_A''' and V_B'''. Such an attractive interaction between $V_O^{\bullet\bullet}$ and the cation vacancies further results in a higher population of the $V_O^{\bullet\bullet}$-containing defect cluster (including $V_O^{\bullet\bullet}$-V_A''' and $V_O^{\bullet\bullet}$-V_B''' in Fig. 2) relative to the isolated $V_O^{\bullet\bullet}$ (red lines in Fig. 2) in air between $T = 1073$–1473 K. This result indicates that modeling of oxygen diffusion in overstoichiometric LMO and LSM has to take into account the associated $V_O^{\bullet\bullet}$-V_A''', $V_O^{\bullet\bullet}$-V_B''', and $V_O^{\bullet\bullet}$-$(V_A'''$-$V_B''')$ species and their potential energy profiles (defect interactions as a function of the defect pair distances) and migration barriers, which requires further computational modeling studies and simulations (not a focus of this work). The influences of the defect interactions to the oxygen diffusivity in bulk LSM can also be supported by the experimental results of similar oxygen diffusivities in the LSM with different A-site deficiency and Sr doping [57], where a different $V_O^{\bullet\bullet}$ concentration is expected from the bulk defect models.

Upon assessment of concentration of the defect complexes in LSM based on the calculated *ab initio* interaction energies and point-defect concentration extracted from the bulk defect model, multiple A-site and B-site cation migration pathways and their barriers are simulated based on the DFT modeling, as we discuss in Sec. IV, which can be incorporated into the random-walk diffusion model formalism to assess the T dependences of the A-site and B-site cation diffusivities in bulk LSM.

IV. CATION DIFFUSION MECHANISM AND MIGRATION BARRIERS

A. A-site cation diffusion mechanisms and migration barriers

The A-site cation diffusion has been previously simulated by De Souza *et al.* [20] using empirical potentials, for a straight-line hop between two nearest-neighbor A sites mediated by a V_A''' [see Fig. 3(a)]. The calculated La_A^x (Sr_A') migration energy is about 3.9 eV (2.9 eV) for LSM at $x = 0$ and increases to 5.3 eV (3.9 eV) at $x = 0.3$. The linear increase in activation energies with increasing Sr_A' concentration was attributed to a combination of steric, electrostatic, and ion polarizability factors. It was pointed out by De Souza *et al.* [20] that a strong correlation exists between the shortest oxygen-oxygen separation versus the calculated A-site migration barriers in the LSM at the orthorhombic or rhombohedral symmetry, suggesting that the distance of octahedral oxygen interstice is a critical parameter which influences the calculated A-site migration barriers.

Explicit A-site cation diffusivities based on the direct V_A''' hopping mechanism in $La_{1-x}Sr_xMnO_{3\pm\delta}$ was further modeled by Puchala *et al.* [29] using KMC simulations in combination with the *ab initio* (A-site) migration energies and defect interaction energies between Sr_A' and V_A''' as a

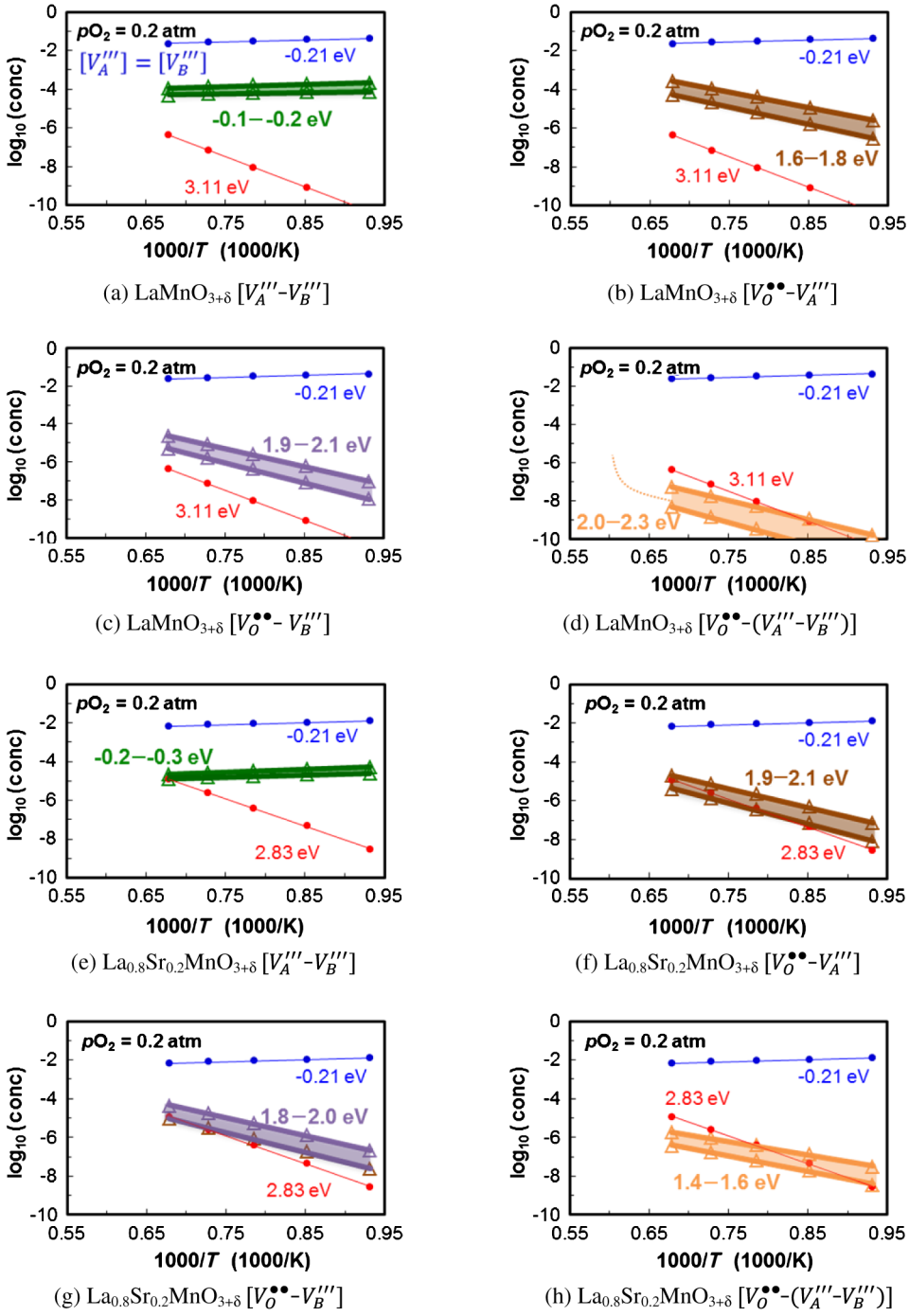

(a) $LaMnO_{3+\delta}$ $[V_A'''\text{-}V_B''']$

(b) $LaMnO_{3+\delta}$ $[V_O^{\bullet\bullet}\text{-}V_A''']$

(c) $LaMnO_{3+\delta}$ $[V_O^{\bullet\bullet}\text{-}V_B''']$

(d) $LaMnO_{3+\delta}$ $[V_O^{\bullet\bullet}\text{-}(V_A'''\text{-}V_B''')]$

(e) $La_{0.8}Sr_{0.2}MnO_{3+\delta}$ $[V_A'''\text{-}V_B''']$

(f) $La_{0.8}Sr_{0.2}MnO_{3+\delta}$ $[V_O^{\bullet\bullet}\text{-}V_A''']$

(g) $La_{0.8}Sr_{0.2}MnO_{3+\delta}$ $[V_O^{\bullet\bullet}\text{-}V_B''']$

(h) $La_{0.8}Sr_{0.2}MnO_{3+\delta}$ $[V_O^{\bullet\bullet}\text{-}(V_A'''\text{-}V_B''')]$

FIG. 2. The calculated concentration of the defect complexes of (a) $[V_A'''\text{-}V_B''']$ (green triangles), (b) $[V_O^{\bullet\bullet}\text{-}V_A''']$ (brown triangles), (c) $[V_O^{\bullet\bullet}\text{-}V_B''']$ (purple triangles), and (d) $[V_O^{\bullet\bullet}\text{-}(V_A'''\text{-}V_B''')]$ (orange triangles) in bulk $LaMnO_{3+\delta}$ as well as (e) $[V_A'''\text{-}V_B''']$, (f) $[V_O^{\bullet\bullet}\text{-}V_A''']$, (g) $[V_O^{\bullet\bullet}\text{-}V_B''']$, and (h) $[V_O^{\bullet\bullet}\text{-}(V_A'''\text{-}V_B''')]$ in bulk $La_{0.8}Sr_{0.2}MnO_{3+\delta}$ at $pO_2 = 0.2$ atm versus $1/T$. The effective formation energies extracted from the slopes are labeled in the figures. The shaded area represents the range of the defect interaction energies based on the values of Table II. For comparison, concentration of $[V_A'''] = [V_B''']$ (blue circles) and $[V_O^{\bullet\bullet}]$ (red circles) versus $1/T$ and their effective formation energies are also included in each figure. All y axes are in the unit concentration (conc) in the $\log_{10}$ scale.

function of defect pair distances. The *ab initio* calculations provided migration barriers of 2.96 and 2.42 eV, for La and Sr in LSM, respectively, which are consistently lower than the empirical potential results. Similar observation is also reported in a very recent DFT-based modeling work of cation diffusion in bulk YSZ [59].

Despite the fact that the *A*-site cation migration barriers of the direct V_A''' hops in the DFT modeling [29] are lower than those of the empirical potential models [20], these DFT barriers are still 1.0–1.5 eV higher than the experimental apparent activation energy of the *A*-site cation (Pr^{3+}) impurity diffusion (approximately 1.3 eV in Ref. [32]). Such a barrier difference between the theoretical values and the experimental measurements raises the question of whether there exist alternative *A*-site diffusion mechanisms that are more favored than the traditional straight-line V_A''' hop. Indeed, mechanisms regarding cation migration in perovskite oxides have been suggested to involve defect clusters [21,31], whereas theoretical modeling of the barriers of the proposed pathways involving the defect clusters remain to be investigated. Therefore, in this work, we consider several possible combinations of a V_A''' with other

point defects as the *A*-site cation transport carriers, including three additional *A*-site cation migration pathways with hopping of V_A''' in the presence of a nearest-neighbor V_B''', $V_O^{\bullet\bullet}$, or $V_B''' - V_O^{\bullet\bullet}$ cluster, as schematically shown in Figs. 3(b)–3(d). The *A*-site cation migration pathway of Fig. 3(d) may be considered as a part of the V_A'''-V_B'''-$V_O^{\bullet\bullet}$ cluster migration mechanism previously proposed by Schulz *et al.* [31] for the $La_{0.9}Sr_{0.1}Ga_{0.9}Mg_{0.1}O_{2.9}$ perovskite. Nonetheless, theoretical barriers for the hopping steps of these cations were not reported in the previous work [31]. Also, the *A*-site cation migration pathways involving the exchange of an *A*-site cation with a nearest-neighbor V_B''' are not included in this work, as formation of such a *B*-site antisite defect is energetically highly unfavorable (approximately 4 eV; see Fig. 1 of Ref. [29]) due to the fact that the ionic radii of the *A*-site cations are too large to occupy the *B*-site in the *B*-O octahedral environment. The calculated DFT La_A^x migration barriers in bulk LMO are summarized in Table III. It can be seen that the La_A^x migration barriers of the pathways, Fig. 3(b) $(V_A'''$-$V_B''')_A$ and Fig. 3(d) $(V_A'''$-V_B'''-$V_O^{\bullet\bullet})_A$, both of which involve a nearest-neighbor V_B''', are at least 1 eV lower than that of the previously explored direct V_A''' hopping mechanism [Fig. 3(a)]. In contrast, the *A*-site cation migration barriers of the diffusion pathways, Fig. 3(c) $(V_A'''$-$V_O^{\bullet\bullet})_A$ and Fig. 3(d) $(V_A'''$-V_B'''-$V_O^{\bullet\bullet})_A$, both of which contain a nearest-neighbor $V_O^{\bullet\bullet}$ in the cation transport carrier, show only a few hundred milli-electron-volt difference as compared to those of the migration pathways without a nearest $V_O^{\bullet\bullet}$ [Fig. 3(a) $(V_A''')_A$ and Fig. 3(b) $(V_A'''$-$V_B''')_A$, respectively], indicating that the presence of a nearest-neighbor $V_O^{\bullet\bullet}$ has a relatively weak influence on the La_A^x migration barriers. The significant reduction in the La_A^x migration barriers in the presence of a nearest-neighbor V_B''' and the weaker influence of the nearest-neighbor $V_O^{\bullet\bullet}$ suggest a reduced electrostatic repulsion between the migrating La (La_{mig}^x) and the nearby Mn_B^x cations (reduced from $4Mn_B^x$ to $3Mn_B^x$ in the presence of a nearest-neighbor V_B''') [60], as well as better accommodation of the $La_{mig}^x - Mn_B^x$ repulsion with a nearest-neighbor V_B''' ($La_{mig} - Mn_B^x$ distances increase from approximately 3.0 to 3.1–3.4 Å with a nearest-neighbor V_B''') in the saddle-image configurations (as shown in Fig. 4). All these contributions are causing the decrease of the *A*-site cation migration barriers in bulk LMO among the investigated *A*-site cation migration pathways.

In addition to the weak influence in the *A*-site cation migration barriers, formation of $V_O^{\bullet\bullet}$ in bulk LSM is energetically unfavorable under SOFC conditions [$V_O^{\bullet\bullet}$ has a (3–4)-eV formation enthalpy] [27]; hence, the *A*-site cation transport in bulk LSM involving a nearest-neighbor $V_O^{\bullet\bullet}$ will not be active in the pO_2 region close to the air due to low transport carrier concentration (see above), which also leads to greater apparent activation energies in the

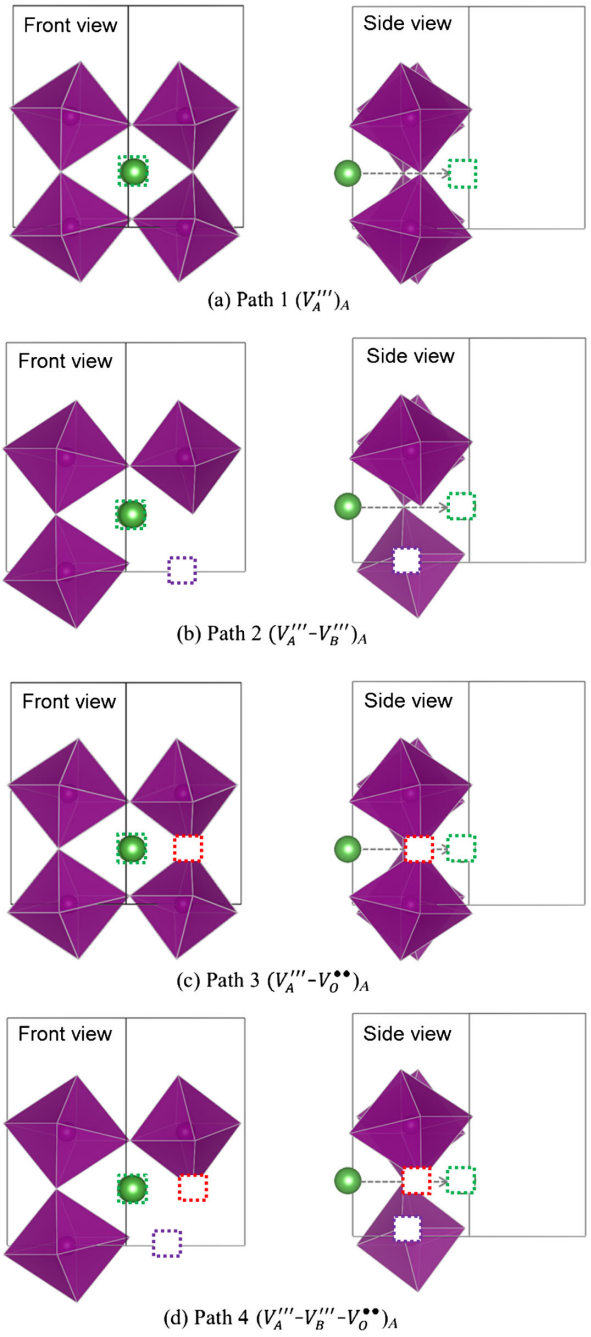

FIG. 3. The schematic illustrations of the investigated *A*-site cation migration mechanisms in bulk LSM created using the VESTA software [58] (same below): (a) the traditional straight-line V_A''' hop $(V_A''')_A$, (b) the V_A''' hop in the presence of a nearest V_B''', $(V_A'''$-$V_B''')_A$, (c) the V_A''' hop in the presence of a nearest $V_O^{\bullet\bullet}$, $(V_A'''$-$V_O^{\bullet\bullet})_A$, and (d) the V_A''' hop in the presence of both a nearest V_B''' and a nearest $V_O^{\bullet\bullet}$, $(V_A'''$-V_B'''-$V_O^{\bullet\bullet})_A$. (a)–(d) The left plots are the front view of the respective migration pathways, and the right plots are the side view of the migration pathways. Green, red, and purple dashed squares represent the V_A''', V_B''', and $V_O^{\bullet\bullet}$, respectively, while the green spheres and the purple octahedra represent La/Sr and Mn-O octahedra in the perovskite lattice.

TABLE III. The DFT La_A^x migration barriers in bulk $LaMnO_3$ for the four diffusion pathways shown in Fig. 3 calculated using three different supercell sizes. For the 80-atom and 160-atom supercell calculations (calcs.), one to six CINEB calculations (specific numbers provided in parentheses) are performed to account for multiple arrangements of the vacancy clusters, and the range of the calculated values are also provided.

La_A^x migration barrier (eV)	80-atom $2\sqrt{2}\boldsymbol{a}_{\text{cubic}}\times 2\sqrt{2}\boldsymbol{a}_{\text{cubic}}\times 2\boldsymbol{a}_{\text{cubic}}$ supercell	160-atom $2\sqrt{2}\boldsymbol{a}_{\text{cubic}}\times 2\sqrt{2}\boldsymbol{a}_{\text{cubic}}\times 4\boldsymbol{a}_{\text{cubic}}$ supercell	320-atom $4\boldsymbol{a}_{\text{cubic}}\times 4\boldsymbol{a}_{\text{cubic}}\times 4\boldsymbol{a}_{\text{cubic}}$ supercell
Path 1 $(V_A'''')_A$ Fig. 2(a)	2.7–3.0 (3 calcs.)	2.6–2.9 (3 calcs.)	3.0 (1 calc.)
Path 2 $(V_A''''\text{-}V_B'''')_A$ Fig. 2(b)	1.3–1.5 (3 calcs.)	1.5–1.6 (3 calcs.)	1.5 (1 calc.)
Path 3 $(V_A''''\text{-}V_O^{\bullet\bullet})_A$ Fig. 2(c)	2.9–3.1 (3 calcs.)	3.0–3.3 (3 calcs.)	...
Path 4 $(V_A''''\text{-}V_B''''\text{-}V_O^{\bullet\bullet})_A$ Fig. 2(d)	1.2–1.9 (6 calcs.)	...	...

predicted *A*-site cation diffusivities (larger slopes in Fig. 2). Nevertheless, a transition in the *A*-site cation transport mechanism from the defect complexes without $V_O^{\bullet\bullet}$ in air to the defect complexes with $V_O^{\bullet\bullet}$ is expected when the oxygen chemical potential conditions change such that the population of the $V_O^{\bullet\bullet}$-containing defect complexes become greater than those without $V_O^{\bullet\bullet}$ (e.g., a sufficiently low pO_2 or under high cathodic overpotential).

To summarize, among the investigated pathways, the *A*-site diffusion pathway of Fig. 3(b) $(V_A''''\text{-}V_B'''')_A$, where the *A*-site cation migration takes place by exchanging a V_A'''' of a $V_A''''\text{-}V_B''''$ cluster with a nearest-neighbor *A*-site cation, is the most active *A*-site cation diffusion mechanism in air at the SOFC operating temperature.

B. The effects of Sr doping on the *A*-site cation migration barrier

The effects of Sr substitution to the *A*-site cation migration barriers are summarized in Fig. 5. It can be seen that the DFT-based La_A^x and Sr_A' migration barriers of the traditional straight-line V_A'''' hop [i.e., path 1 $(V_A'''')_A$] and the most active *A*-site cation migration pathway of the V_A'''' hop of a $V_A''''\text{-}V_B''''$ cluster [i.e., $(V_A''''\text{-}V_B'''')_A$] exhibit a weaker dependence on the Sr_x concentration ($x = 0.0$–0.25) than the empirical potential results reported in Ref. [20]. A similar trend is also found in the calculated *B*-site cation migration barriers below (see Table IV). The weaker Sr concentration dependence in the *A*-site cation migration energies in this study may be attributed to a more delocalized charge description in DFT modeling than that provided by empirical potentials [20].

C. Trends in the *A*-site cation migration barriers versus metal types

In addition to the La_A^x and Sr_A' migration barriers, several other metal cations used in solid electrolyte materials for the SOFC applications such as Y_A^x, Gd_A^x, and $Zr_A^{\bullet}$ are also investigated to understand the trends of the cation migration barriers versus cation types in bulk LSM/LMO. These metal cations possess not only different ionic radii but also different ionic charges, both of which may lead to differences in the calculated *A*-site cation migration barriers. Here we focus on distinguishing these fundamental factors through the trends of the *A*-site cation migration barriers versus the metal cation types in bulk LMO based on the most active $V_A''''\text{-}V_B''''$ migration pathway shown in Fig. 2(b) and the traditional V_A'''' hop mechanism shown in Fig. 2(a).

As we discuss in Sec. III A, there is at least an approximately 1 eV difference in the calculated *A*-site cation migration barriers between the most active V_A'''' hop of a $V_A''''\text{-}V_B''''$ cluster pathway [Fig. 3(b)] and the traditional V_A'''' hop mechanism [Fig. 3(a)]. When comparing the trends of the migration barriers among various metal cations, these two *A*-site cation migration pathways show similarity in their correlations. Specifically, the barriers increase with (1) increasing cationic charge and (2) increasing the ionic radii at a given ionic charge, as shown in Fig. 6.The ionic charge dependence of the migration barriers further supports the role of the electrostatic repulsion between the migrating *A*-site cations (A_{mig}) and the nearby Mn_B^xs in the saddle-point image to be a main factor governing the *A*-site cation migration barriers, since the calculated migration barriers correlate with the formal charge states of the cations $Zr_A^{\bullet}$, La_A^x, and Sr_A' (i.e., 4+, 3+, and 2+, respectively). In addition, due to the different charge doping of the cations, local charge redistribution (and, hence, modification of the nearby Mn—O bonds) occurs near the migrating cation, leading to different degrees of relaxation for the compressive strain imposed to the A_{mig}-O-Mn_B^x shell in the saddle-point configuration. Specifically, upon hole doping (e.g., Sr_A'), local charge rehybridization shortens the Mn—O bonds around the A_{mig} impurity, which relieves the strain to the A_{mig}—O bonds in the saddle-point image and *vice versa* for the $Zr_A^{\bullet}$ in the case of electron doping. For a given charge state and different radii (i.e., La_A^x, Gd_A^x, and Y_A^x), the trend in the migration barrier is attributed to different degree of steric hindrance (or strain) imposed to the A_{mig}—O bonds in the saddle-point image, and the slight

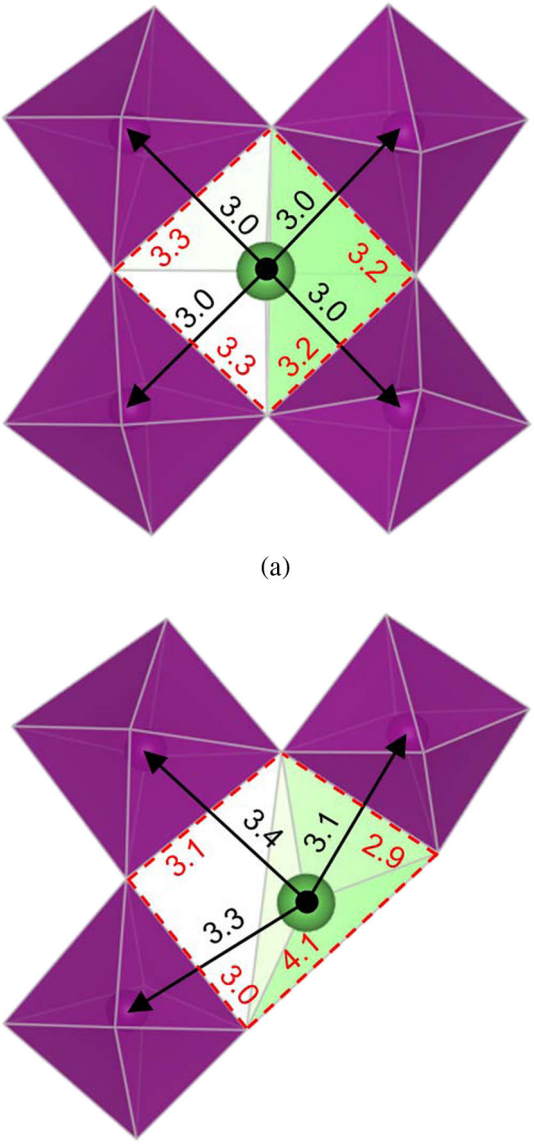

FIG. 4. The saddle-point configurations of the investigated *A*-site cation migration mechanisms in bulk LSM: (a) the traditional straight-line V_A''' hop $(V_A''')_A$, and (b) the V_A''' hop at the presence of a nearest V_B''', $(V_A'''\text{-}V_B''')_A$. Green spheres and the purple octahedra represent La/Sr and Mn-O octahedra in the perovskite lattice. The La_{mig}-Mn_B^x distance are labeled with black solid arrows and corresponding numbers in black font (unit: Å), whereas the nearest octahedral O-O interstices are labeled with red dashed lines and numbers in red font (unit: Å).

differences in the A_{mig}—O hybridization result only in insignificant modification of the nearby Mn—O bonds [61]. It is noted that the opposite trend of cation migration barriers versus the ionic radii exists between the group of $Zr_A^{\bullet}$, La_A^x, and Sr_A' and the group La_A^x, Gd_A^x, and Y_A^x, which suggests that the electrostatic (ionic charge) factor overrides the steric (ionic radius) factor when the formal cationic charge is varied.

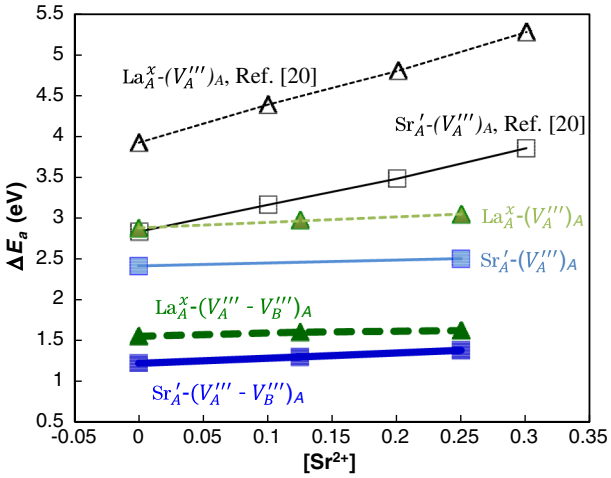

FIG. 5. *A*-site cation migration energies as a function of Sr-doping concentration in $La_{1-x}Sr_xMnO_3$ for the migration pathways of $(V_A''')_A$ and $(V_A'''\text{-}V_B''')_A$. The black open symbols are taken from the empirical potentials simulations in Ref. [20], whereas the solid symbols are the migration barriers are calculated using DFT in this work. Triangle and square data points represent the simulated La and Sr migration energies via a direct hop to the first nearest-neighbor *A*-site vacancy. It can be seen that the DFT migration energies obtained in this work (solid symbols) are consistently lower than those reported in Ref. [20] based on the empirical potentials and both exhibit different slopes versus Sr concentration.

D. *B*-site cation migration mechanisms and barriers

For the *B*-site cation transport in bulk LSM, six migration pathways are considered, as schematically illustrated in Fig. 7. The *B*-site cation migration mechanisms of paths 1–3 are simulated with empirical potentials by De Souza *et al.* [20], and are investigated again in this work based on DFT modeling. The migration path 4 $(V_O^{\bullet\bullet}\text{-}V_B''')_B$ is a first nearest-neighbor V_B''' hop that is available when a $V_O^{\bullet\bullet}$ is formed in the middle of the direct V_B''' hopping pathway. The migration paths 5 and 6, both of which contain the same defect complexes $V_A'''\text{-}V_B'''\text{-}V_O^{\bullet\bullet}$ as the *B*-site cation transport carriers, differ in their hopping pathways as follows: Path 5 is analogous to path 1 with addition of a nearest-neighbor $V_O^{\bullet\bullet}$, whereas path 6 is analogous to path 4 with addition of a nearest V_A'''. It is noted that path 5 has also been proposed by Schulz *et al.* [31] as one hopping step of the $V_A'''\text{-}V_B'''\text{-}V_O^{\bullet\bullet}$ migration mechanism. We note that there are no explicit theoretical barriers reported for this cation hopping step suggested originally in Ref. [31].

Table IV summarizes the calculated barriers of the six *B*-site cation migration pathways investigated in this work, along with those reported in Ref. [20] using the empirical potentials method. Although the trend of the migration barriers for paths 1–3 is consistent between the two modeling methods, the DFT migration barriers are significantly lower than those simulated with empirical potentials. Comparing all the DFT-based *B*-site cation migration

TABLE IV. Summary of the migration barriers of the four *B*-site diffusion pathways calculated in this work versus those reported in Ref. [20].

Mn migration barrier (eV)		$x = 0.0$	$x = 0.25$
Path 1 $(V_A'''\text{-}V_B''')_B$	Ref. [20]	3.5	~5.0
	This work (DFT)	1.5–2.0	1.7–2.3
Path 2 $(\text{curved}V_B''')_B$	Ref. [20]	7.7–10.6	10–11
	This work (DFT)	4.4	4.5
Path 3 $(2\text{NN}V_B''')_B$	Ref. [20]	14–15	⋯
	This work (DFT)	8.4	8.6
Path 4 $(V_O^{\bullet\bullet}\text{-}V_B''')_B$	Ref. [20]	⋯	⋯
	This work (DFT)	3.9	4.0
Path 5 $(V_A'''\text{-}V_B'''$ with $V_O^{\bullet\bullet})_B$	This work (DFT)	2.5	2.6
Path 6 $(V_O^{\bullet\bullet}\text{-}V_B'''$ with $V_A''')_B$	This work (DFT)	2.0	2.3

barriers in Table IV, it can be seen that among the six *B*-site cation migration pathways, those exhibiting lower barriers are the following: path 1 $(V_A'''\text{-}V_B''')_B$, path 5 $(V_A'''\text{-}V_B'''$ with $V_O^{\bullet\bullet})_B$, and path 6 $(V_B'''\text{-}V_O^{\bullet\bullet}$ with $V_A''')_B$, all of which involve a nearest-neighbor $V_A'''\text{-}V_B'''$ cluster as the cation transport carrier or a part of the transport defect complex. Again, for the pathways involving $V_O^{\bullet\bullet}$ as part of the *B*-site cation transport carrier, namely, path 5 $(V_A'''\text{-}V_B'''$ with $V_O^{\bullet\bullet})_B$, path 6 $(V_B'''\text{-}V_O^{\bullet\bullet}$ with $V_A''')_B$, and path 4 $(V_O^{\bullet\bullet}\text{-}V_B''')_B$, an additional energy cost for oxygen-vacancy formation in bulk LSM needs to be added in evaluation of apparent activation energies of the cation tracer and self-diffusivities in air, since the large $V_O^{\bullet\bullet}$ formation energy cannot be fully offset by its binding energy to the cation vacancies. Consequently, under typical SOFC operating conditions, the DFT energetic results suggest that path 1 $(V_A'''\text{-}V_B''')_B$ is the most active *B*-site cation migration pathway in bulk LSM among the six investigated mechanisms.

Considering Mn_B^x migration to the neighboring *B* sites, path 1 $(V_A'''\text{-}V_B''')_B$ can have three distinct migration passages, which are labeled as 1NN, 2NN, and 3NN in Fig. 7(a). These three passages have the same Mn migration distances along the paths, while the resulting Mn_B^x positions are distinct in terms of their distances to the original Mn_B^x in the initial state. The results suggest that the 1NN Mn_B^x migration of path 1 $(V_A'''\text{-}V_B''')_B$ has a higher barrier (1.9–2.0 eV), whereas 2NN and 3NN Mn_B^x migration barriers are comparable (1.5–1.6 eV), as shown in Fig. S6 of Ref. [45]. The states of the two energy peaks (with the higher one defined as the saddle-point configuration) in the potential energy profiles of path 1 $(V_A'''\text{-}V_B''')_B$ are associated with a trigonal planar Mn-O configuration in which the migrating Mn (Mn_{mig}) is located at the center of three nearest oxygens that originally form one of the faces of the Mn-O octahedra, as shown in Fig. 8. The (1.5–2.0)-eV Mn migration barriers result from the low (trigonal) Mn-O coordination in the saddle-point configuration as well as from the steric hindrance to the Mn_{mig} when crossing the smallest oxygen triangle (i.e., a face of the Mn-O octahedra) in the perovskite lattice. The removal of one of the trigonal plane oxygens does not lead to a decrease of the migration barriers (i.e., path 5), due to destabilization of the Mn_{mig} when placed in a two-oxygen-coordinated environment, which counterbalances the relieved steric hindrance. The (0.3–0.5)-eV higher migration barriers of the 1NN Mn_B^x migration (Table S2 of Ref. [45]) are associated with the spatial arrangement of the V_B''' and the Mn_{mig}, which leads to a terminal oxygen hybridized with one Mn_{mig} (and a short Mn—O bond of approximately 1.8 Å) in the initial state, thereby causing enhanced steric hindrance to the Mn_{mig} due to the shorter O-O distances of the trigonal face of the Mn-O octahedra. Therefore, these DFT modeling results suggest that Mn_B^x path 1 $(V_A'''\text{-}V_B''')_B$ migration between the second and third nearest-neighbor *B* sites is intrinsically more active than between the first nearest-neighbor *B* sites.

The local minimum with an energy of 1.0 eV and, respectively, 1.5 eV, relative to the initial and final states between the two energy peaks in the potential energy profile corresponds to the Mn_A^x state (the Mn *A*-site antisite defect). The stability and concentration of the Mn_A^x defect can be dependent on the A/B ratio and the Mn_3O_4 activity [54,55], but it is confined in the adopted LSM bulk defect model with the artificial constraint of a fixed A/B ratio (equal to 1). A variation of the Mn_A^x population can potentially result in alternative active pathways for the Mn transport on the *A*-site lattice in bulk LSM, a topic which is further discussed in the next section.

Overall, at the cation stoichiometry of the A/B ratio equal to 1, these DFT modeling results show that among the six migration pathways investigated in this work, the lowest barrier for Mn corresponds to path 1 $(V_A'''\text{-}V_B''')_B$. This result also supports a previously proposed active Mn migration mechanism in overstoichiometric LSM [15,32]. Our results also demonstrate that migration of Mn between the first nearest-neighbor *B* sites for path 1 $(V_A'''\text{-}V_B''')_B$ is not as active as those between the second and third nearest-neighbor *B* sites, due to the presence of an undercoordinated terminal oxygen that causes enhanced steric hindrance to the Mn_{mig}. Given that the DFT-based $\text{Mn}_B^x(V_A'''\text{-}V_B''')_B$ migration barriers (1.5–1.6 eV) are comparable to the $\text{La}_A^x(V_A'''\text{-}V_B''')_A$ migration barriers, approximately 1.6 eV, and that both pathways involve the same cation transport carriers of $V_A'''\text{-}V_B'''$, the corresponding apparent activation energies of the Mn_B^x $(V_A'''\text{-}V_B''')_B$ and $\text{La}_A^x(V_A'''\text{-}V_B''')_A$ diffusion coefficients are predicted to be comparable based on the three-dimensional random-walk formalism, i.e., approximately 1.4 eV (as shown in Fig. 10).

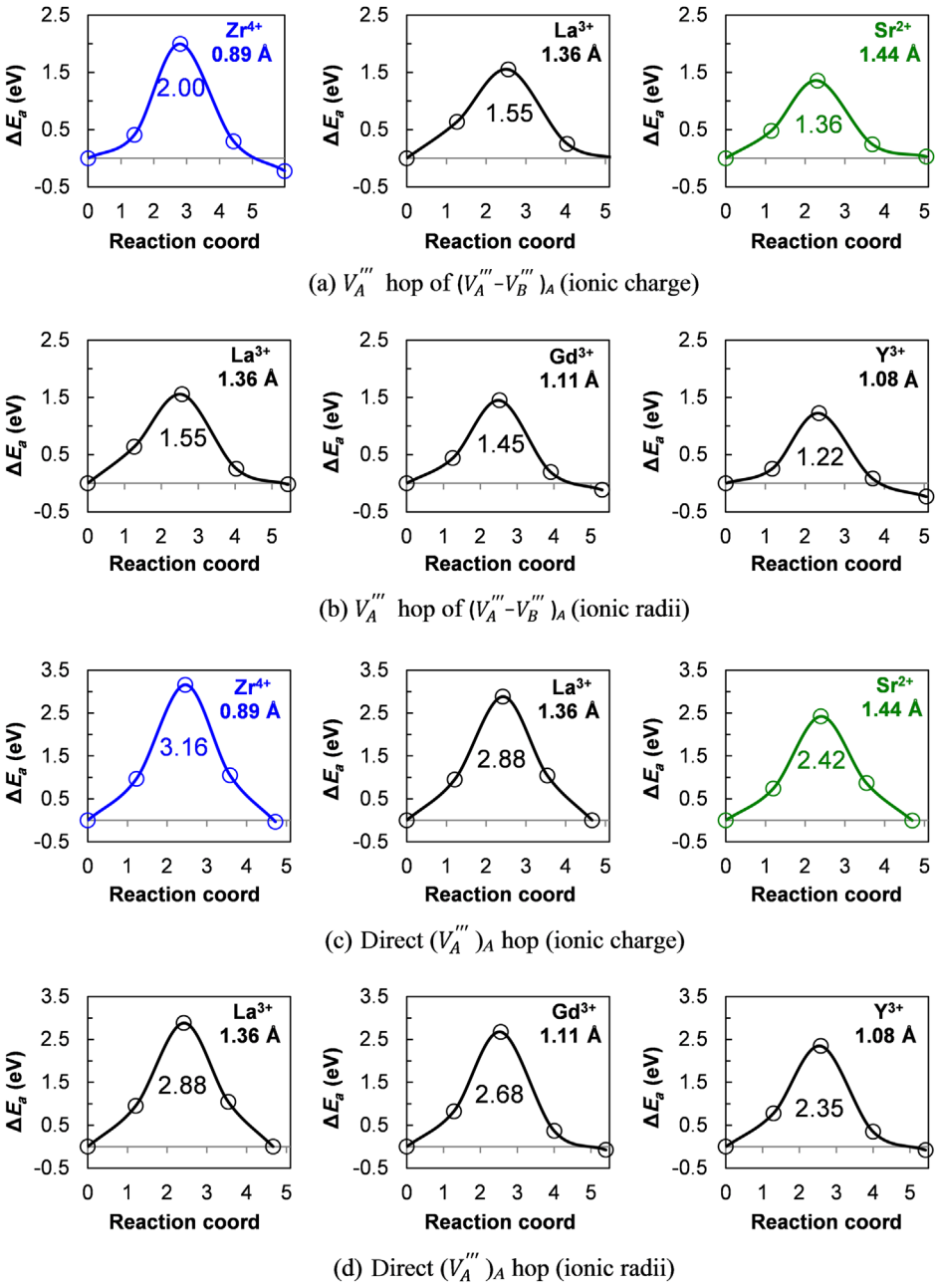

(a) V_A''' hop of $(V_A'''\text{-}V_B''')_A$ (ionic charge)

(b) V_A''' hop of $(V_A'''\text{-}V_B''')_A$ (ionic radii)

(c) Direct $(V_A''')_A$ hop (ionic charge)

(d) Direct $(V_A''')_A$ hop (ionic radii)

FIG. 6. The variations of the A-site cation migration barriers for the $(V_A'''\text{-}V_B''')_A$ pathway [Fig. 3(b)] versus (a) ionic charge and (b) ionic radii at a specific cation oxidation state of 3+, and for the $(V_A''')_A$ pathway [Fig. 3(a)] versus (c) ionic charge and (d) ionic radii at a formal charge state. The Shannon ionic radius of each cation as provided in Ref. [62] is indicated in the top right corner of each figure. The colors of blue, black, and green of the lines and fonts in the figures are used to represent the cation formal charge states of 4+, 3+, and 2+, respectively.

However, the experimental values provided in Refs. [16,17] for Mn diffusion are lower in activation energy by approximately 1 eV, suggesting that the existence of alternative Mn diffusion pathways not presently described in the Mn_B^x $(V_A'''\text{-}V_B''')_B$ diffusion model. Below, we discuss the transport of the Mn_A^x species as an active pathway for the Mn diffusion in bulk LSM and LMO, which might explain the very low measured activation energy [16,17].

E. Mn_A^x cation migration mechanism and barriers

The existence of the Mn_A^x species has been suggested in the literature based on structural characterizations, magnetic measurements, and oxygen nonstoichiometry, particularly for the A-site-deficient LSM [54,55,63,64]. Nakamura [54] revised the bulk LMO defect model and suggested that Mn_A^x concentrations of 0.01 and 0.03 can exist in the A-site-deficient LMO with an A/B ratio of 0.96 and 0.92, respectively. Grundy *et al.* [55] used the calculation of phase diagrams (CALPHAD) approach to model oxygen nonstoichiometry of LMO at varying A/B cation ratios and concluded that inclusion of the Mn_A^x species in the CALPHAD model is necessary to reproduce the experimental $La_{0.9}MnO_{3+\delta}$ oxygen nonstoichiometry at the SOFC operating temperature. In the first-principles-based LMO defect modeling [27], it was also shown that stability of the Mn_A^x exhibits a low enough energy (approximately 1 eV) that potentially plays a role in

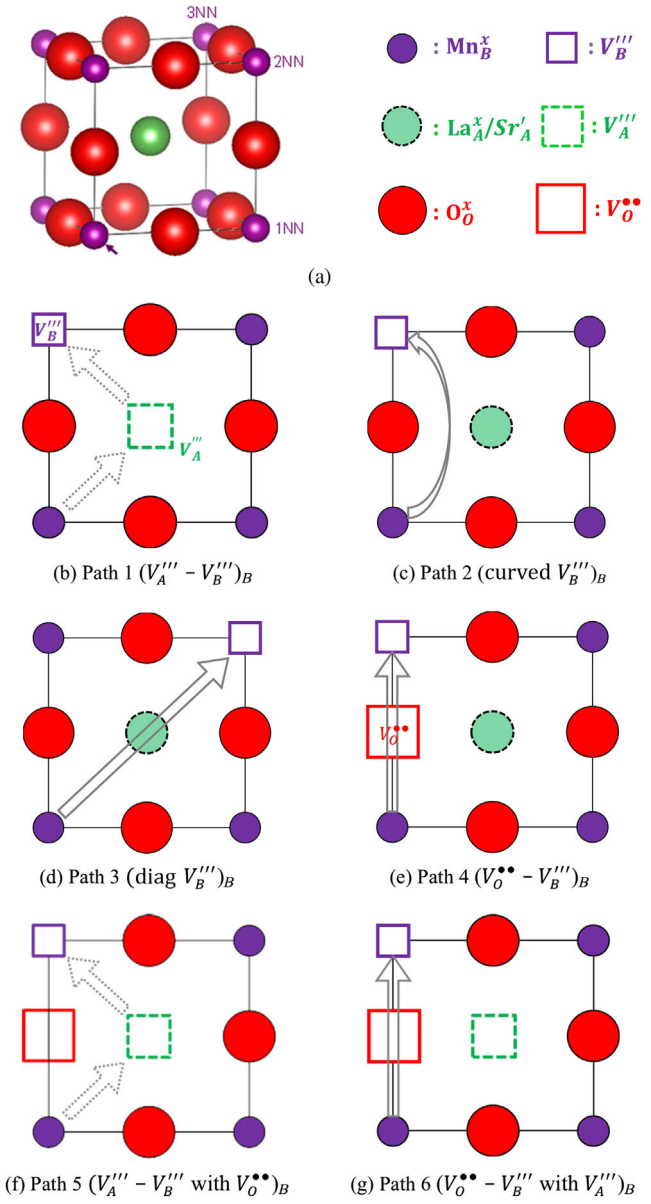

FIG. 7. (a) A schematic (La, Sr)MnO_3 perovskite crystal created using the VESTA software [58]. The red, purple, and green spheres represent the oxygen, *B*-site, and *A*-site cations, whereas the open squares in the corresponding colors are used to represent vacancies. These symbols are used in (b), (c), (d), (e), (f), and (g) to describe the six Mn migration pathways considered in this work, which are labeled as path 1 $(V_A'''\text{-}V_B''')_B$, path 2 (curved $V_B''')_B$, path 3 (diag$V_B''')_B$, path 4 $(V_O^{\bullet\bullet}\text{-}V_B''')_B$, path 5 $(V_A'''\text{-}V_B'''$ with $V_O^{\bullet\bullet})_B$, and path 6 $(V_O^{\bullet\bullet}\text{-}V_B'''$ with $V_A''')_B$, respectively (the subscript *B* of the brackets denotes the *B*-site cation migration). The purple arrow indicates the Mn_B^x in the initial state before migration, whereas three types of symmetry distinct *B* sites are labeled as 1NN, 2NN, and 3NN in (a). It is noted that the green solid spheres and the green open squares are drawn with dashed lines in (b)–(g), to indicate that the *A*O layer is located above or beneath the BO_2 plane in a top-view projection along the $\langle 100\rangle_{\text{perovskite}}$ direction. Dotted arrows are used in (b) and (f) to indicate an interlayer Mn migration between the *A*O and BO_2 planes.

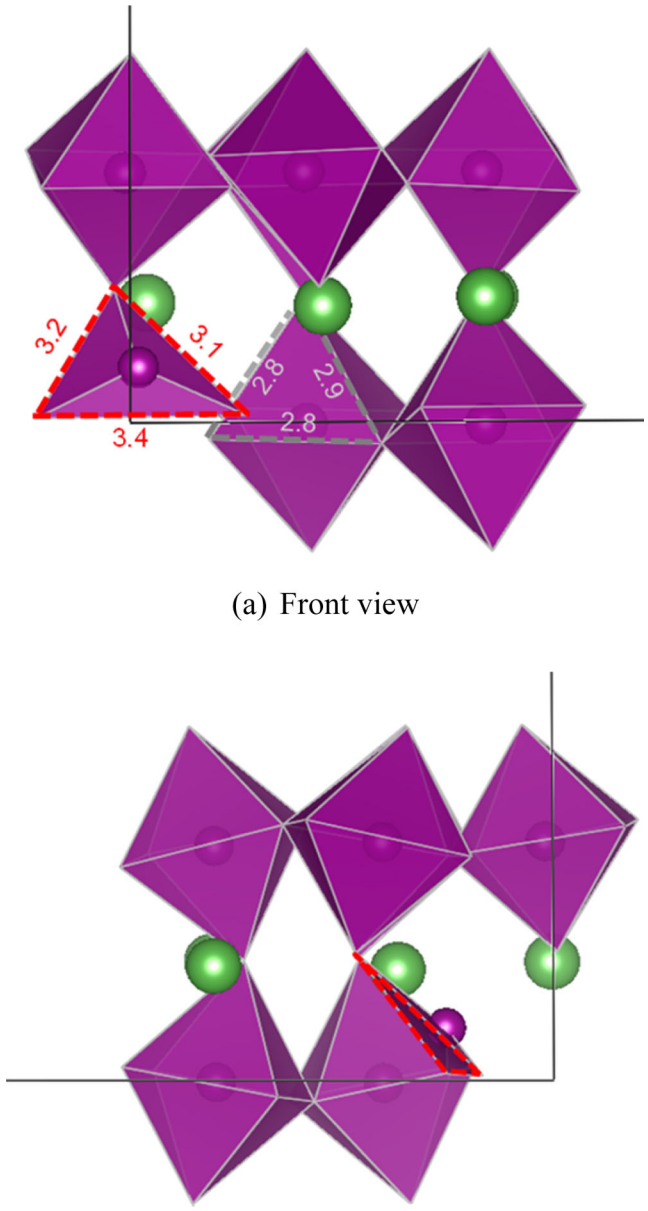

FIG. 8. (a) Front view and (b) side view of the saddle-point image for the Mn migration pathway of $(V_A'''\text{-}V_B''')_B$ shown in Fig. 7(b). The red dashed lines highlight the O-O interstices of the trigonal planar Mn-O, with the red numbers indicating the O-O distances. A typical O-O interstice and their O-O distances of the Mn-O octahedra are also provided in panel (a) indicated with gray dashed lines and gray font.

the LMO bulk defect chemistry. Since the A/B cation ratio in LSM may not be well controlled in the experimental synthesis and measurements [65], deviation of the A/B cation ratio from 1 can lead to changes of the Mn_A^x concentration. Its influences on the overall Mn cation diffusivities are less clear.

As a first step to probe the Mn_A^x diffusivity, we calculate the Mn_A^x migration barrier of a first nearest-neighbor Mn_A^x-V_A''' hop. Figure 9 shows the calculated potential energy profile of the Mn_A^x migration to a nearest-neighbor V_A''', as well as the initial state, saddle-point image, and the final-state configurations. The saddle-point configuration is analogous to that of the simple V_A''' hopping for the A-site cation migration [Fig. 4(a)], and the O-O distances of the square-planar Mn-O are approximately 3.0 Å, which are shorter than those of Fig. 4(a), i.e.,3.2–3.3 Å. The calculated migration barrier of the Mn_A^x-V_A''' hop is found to be approximately 0.5 eV, significantly lower than the barrier of the active $Mn_B^x(V_A'''$-$V_B''')_B$ migration pathway under the constraint of A/B ratio equal to 1, which suggests the $Mn_A^x(V_A''')_A$ pathway on the A-site lattice can potentially be activated in parallel to the $Mn_B^x(V_A'''$-$V_B''')_B$ migration pathway when the population of Mn_A^x is increased in LSM (e.g., with A-site deficiency). In the Mn tracer diffusion study reported by Miyoshi and Martin [16], a tracer layer of the radioactive isotope ^{54}Mn is added to the surface of the LMO substrate (the LMO substrate has a nominal composition of $LaMnO_{3\pm\delta}$ with the A/B ratio equal to 1), which causes a perturbation to the A/B ratio in the shallow region near the surface. Therefore, one may expect an increase of Mn_A^x concentration due to the A-site deficiency, leading to a low experimental apparent activation energy of 0.6 eV in the extracted Mn tracer diffusion coefficients. To quantify the influences of the A-site deficiency to the Mn diffusivities in bulk LSM, further work is needed to develop an improved diffusion modeling which includes the Mn_A^x species in the bulk defect model and the associated defect energetics and migration barriers of all possible Mn migration pathways in LSM at varying A/B ratios. Careful experimental cation diffusivity measurements with characterization of the cation nonstoichiometry are also needed for making comparison with such theoretical modeling.

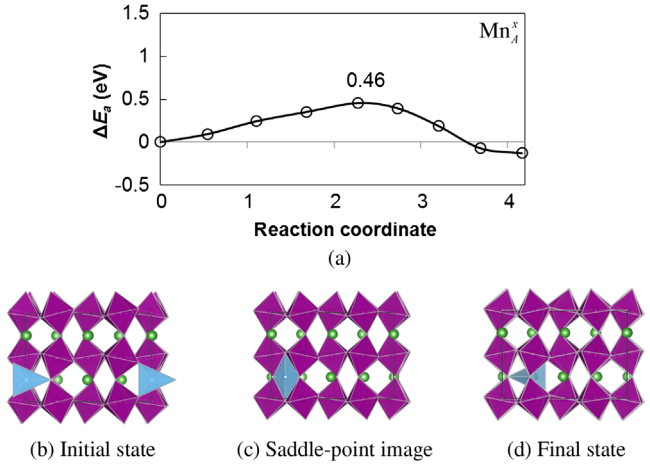

FIG. 9. (a) The potential energy profile of the Mn_A^x migration to the first nearest-neighbor V_A''', (b) the initial state configuration, (c) the saddle-point image, and (d) the final-state configuration. The Mn-O polyhedral of the migrating Mn cation is presented in the cyan color. The O-O distances of the square-planar Mn-O in the saddle-point image are approximately 3.0 Å.

V. TEMPERATURE AND STRONTIUM-DOPING DEPENDENCES OF LSM CATION SELF-DIFFUSION COEFFICIENT

In this section, the DFT-based defect energetics and migration barriers of the most active cation migration pathways in bulk LSM are incorporated in a three-dimensional random-walk formalism to assess the temperature dependences of the cation diffusion coefficients. It is noted that the A/B cation ratio is fixed in the LSM bulk defect model. The absolute quantities of the modeled cation diffusion coefficient that we show below are based on fitting to the experimental cation diffusion coefficients in the Arrhenius expression with the prefactor A, as we describe in Sec. II C. The fitted value is $A = 5.17 \times 10^{12}$, which is physically reasonable for the parameters involved in A [51]. Specifically, the fitting is performed only to the experimental A-site cation diffusivities, as the experimental Mn diffusivities may be sensitive to variation of the A/B cation ratio. The fitted parameters of the D_{La}^* are then directly transferred to calculate the D_{Mn}^*. In principle, the refinement of the tracer correlation factors may be assessed by Monte Carlo simulations or analytical formulation with frequencies for relevant vacancy jumps of the diffusion pathways. However, given the complex energy landscapes and the new active cation diffusion pathways uncovered in this study, such an assessment is beyond the scope of this work, and an assumption is made in the cation tracer diffusivity analysis below that the tracer correlation factor exhibits a weak temperature dependence, and, therefore, the major temperature dependences in the tracer cation diffusivities come from the defect energetics for the associated transport carriers as well as the corresponding migration barriers. The main purpose of this analysis is to convert the DFT-based energetics and migration barriers of the active cation migration pathways into estimates of D_{La}^* and D_{Mn}^*, to allow direct comparison of the temperature dependences with the available experimental results.

A. Apparent activation energies of the $LaMnO_{3\pm\delta}$ cation self-diffusion coefficients

Figure 10 shows the calculated LMO cation tracer diffusion coefficients of D_{La}^* and D_{Mn}^* as a function of $1000/T$, along with the experimental cation diffusivity results reported in the literature [15–17,32]. Upon incorporation of the (1.5–1.6)-eV migration barrier of the $La_A^x(V_A'''$-$V_B''')_A$ pathway, the obtained apparent energy of the D_{La}^* is 1.4 eV, which agrees very well with the experimental apparent activation energy of the Pr impurity diffusivity in bulk LMO (1.3 eV) [32]. The calculated DFT migration barrier of $Pr_A^x(V_A'''$-$V_B''')_A$ is close to that of

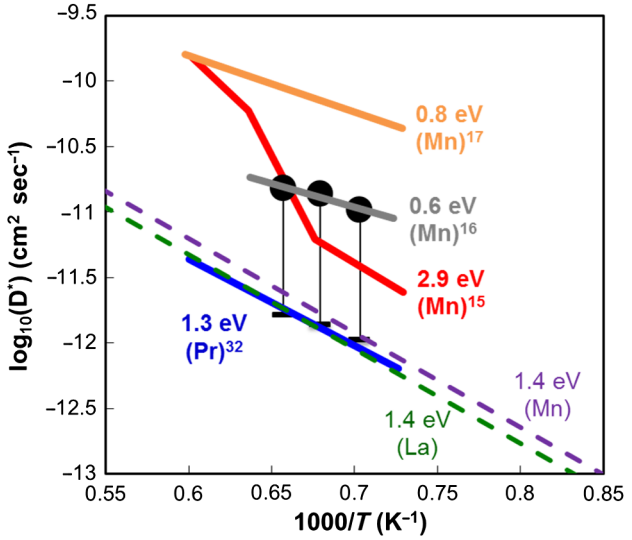

FIG. 10. Logarithm of the modeled cation tracer diffusion coefficients versus $1000/T$ for D^*_{La} (green dashed and dotted lines) and D^*_{Mn} (purple dashed and dotted lines) in bulk $LaMnO_{3\pm\delta}$. The data of the experimental Mn tracer or self-diffusion coefficients are taken from Ref. [16] (black filled circles with error bars and the gray solid line), Ref. [15] (the red solid line), and Ref. [17], as well as the Pr impurity diffusion coefficients reported in Ref. [32] (the blue solid line) are included for comparison. We note that even though the same fitting parameters are used to calculate D^*_{Mn}, the slightly higher magnitude of the calculated D^*_{Mn} versus D^*_{La} reflects on their different hopping paths and distances. The active pathway of $Mn^x_B(V'''_A\text{-}V'''_B)_B$ takes place via the second and third nearest-neighbor B sites versus the first nearest-neighbor A sites of the $La^x_A(V'''_A\text{-}V'''_B)_A$ pathway, as shown Figs. S6 of Ref. [45] versus Fig. 3(b).

$La^x_A(V'''_A\text{-}V'''_B)_A$ (approximately 1.6 eV), due to their similar ionic radii [62]. It is noted that the apparent activation energy of 1.4 eV of D^*_{La} is comparable to the calculated $La^x_A(V'''_A\text{-}V'''_B)_A$ migration barrier, approximately 1.5 eV (path 2 of Table III). This is due to the slightly negative effective formation energy of $[V'''_A\text{-}V'''_B]$ shown in Fig. 2(a). Furthermore, the D^*_{Mn} is slightly higher than D^*_{La} in the diffusivity modeling, which is a result of greater hopping distance along the 2NN and 3NN hops of the migration pathways of $Mn^x_B(V'''_A\text{-}V'''_B)_B$ than those of $La^x_A(V'''_A\text{-}V'''_B)$.

In addition to the experimental apparent activation energy of LMO D^*_{Mn} reported in Ref. [16], two other experimental studies are also included in Fig. 10 for comparison, i.e., the solid-state reaction between La_2O_3 and Mn_3O_4 [15] and the diffusion couple of LMO and $LaCoO_3$ [17]. A significantly higher activation energy of 2.9 eV for the Mn diffusion coefficients from Ref. [15] versus the 0.6 eV of Ref. [16] and 0.8 eV of Ref. [17] was suggested by Palcut *et al.* [17] to be due to different defect population in the perovskite phase formed in the solid-state reaction (with unequal cation-vacancy concentrations) versus the sintered LMO in the tracer diffusion or diffusion couple experiments. The D^*_{Mn} extracted from the solid-state reaction results [15] may not be well described by the modeled bulk D^*_{Mn}, as factors such as the chemical inhomogeneity in LMO or participation of grain-boundary transport are not included in the current bulk diffusion model. The D^*_{Mn} extracted from the diffusion couple measurements [17] are the extrapolated values to the LMO end member, and their magnitudes are about 1 order higher than those of Ref. [16], whereas the apparent activation energy of 0.8 eV is close to that of the 0.6 eV reported by Miyoshi and Martin [16]. The experimental apparent activation energies of 0.6–0.8 eV for D^*_{Mn} are now within the range of the two active Mn migration mechanisms that we discuss in Sec. IV: 1.5–1.6 eV for the $Mn^x_B(V'''_A\text{-}V'''_B)_B$ pathway and 0.5 eV for the $Mn^x_A(V'''_A)_A$ pathway. Note that only the D^*_{Mn} of the $Mn^x_B(V'''_A\text{-}V'''_B)_B$ pathway is included in Fig. 10, which can be regarded as a lower bound of the modeled D^*_{Mn} for the scenario of the A/B cation ratio equal to 1. The potentially more active pathway $Mn^x_A(V'''_A)_A$ requires further in-depth modeling due to the experimental uncertainty in the A/B ratio and the coupling of the $La^x_A(V'''_A\text{-}V'''_B)_A$ transport. Still, by comparing the lower bound D^*_{Mn} results predicted in this work with the experiments, the extracted activation energy of D^*_{Mn} for the $Mn^x_B(V'''_A\text{-}V'''_B)_B$ pathway is now in better agreement than the previous empirical potentials simulation results [20].

B. LSM cation self-diffusion coefficients versus Sr substitution level

Figure 11 shows the predicted D^*_{La} in LSM at $x = 0.0$ (thick green dashed lines), $x = 0.2$ (thin light green dashed lines), and $x = 0.3$ (olive dotted line) as well as their apparent activation energies, along with the experimental A-site cation diffusion coefficients reported in the literature (thick solid blue line) [32]. An assessment of D^*_{La} at $x = 0.3$ is performed using the experimental oxygen overstoichiometry data versus T at $P(O_2) = \sim 1$ bar from Ref. [23], with the calculated $V'''_A\text{-}V'''_B$ interaction energy of 0.3 eV from Table II and a $La^x_A(V'''_A\text{-}V'''_B)_A$ migration barrier of approximately 1.7 eV from Table S2 of Ref. [45] (the adopted experimental oxygen nonstoichiometry data and the predicted $V'''_A\text{-}V'''_B$ concentration are provided in Table S4 of Ref. [45]). The purpose of this assessment is to examine how the A-site cation diffusivities in bulk LSM are quantitatively influenced by change of the Sr substitution level. Here, the comparison is mainly focused on the A-site cation diffusivities, since the B-site cation diffusivities may vary depending on the A/B ratio.

In Fig. 11, D^*_{La} of LSM at $x = 0.3$ (dotted olive line) is lowered by approximately 2.5 orders, and D^*_{La} of LSM at $x = 0.2$ (dotted olive line) is lowered by approximately 1 order, as compared to D^*_{La} of LSM at $x = 0.0$. All the D^*_{La} between $x = 0.0$–0.3 exhibit comparable apparent activation energies of 1.4–1.6 eV. It is noted that due to the use of

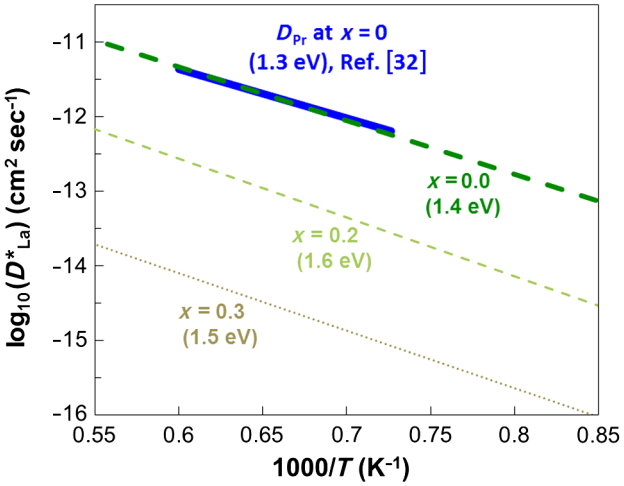

FIG. 11. Logarithm of the model predicted D^*_{La} versus $1000/T$ for La (green lines) in bulk LSM at $x = 0.0$ (thick green dashed lines), $x = 0.2$ (thin light green dashed line), and $x = 0.3$ (olive dotted line). The blue thick line corresponds to the experimental $LaMnO_{3\pm\delta}$ Pr impurity diffusion coefficient results adapted from Ref. [32]. The activation energies extracted from the slopes are also indicated in the figure.

the same V'''_A-V'''_B defect interaction energy and the same migration barrier for $x = 0.2$ and $x = 0.3$ (based on the Sr-doping concentration of the simulated LSM supercell at $x = 0.25$), a 0.1 decrease of the apparent activation energy of D^*_{La} at $x = 0.3$ versus $x = 0.2$ is a result of the variation with temperature of the cation-vacancy concentration and, therefore, of the equilibrium oxygen nonstoichiometry. It is likely there is a small increase (approximately 0.1–0.2 eV) in the migration barrier due to shortened Mn—O bond length upon increasing x from $x = 0.2$ to $x = 0.3$ (which results in an enhanced steric constraint to the migrating cations). This enhanced steric constraint may further lead to a slightly lower D^*_{La} with a slightly higher apparent activation energy for $x = 0.3$, but it cannot be resolved here due to the coarse Sr concentration grid of the simulated supercells in the DF modeling.

Since the effective formation energies (slopes of $1/T$ dependences) of V'''_A, V'''_B, and the defect clusters V'''_A-V'''_B extracted from the LSM bulk defect models at $x = 0.0$–0.3 are shown to be close to 0 [see Fig. 2(a) versus Fig. 2(e) and Table S3 of Ref. [45]], while their concentrations differ by 0.5–1 orders of magnitude. Therefore, the overall effects of Sr'_A doping to the D^*_{La} in bulk LSM shown in Fig. 11 can be attributed to decrease of the cation transport carrier concentrations, i.e., a lower concentration of the V'''_A-V'''_B clusters with increasing x for the A-site cation migration mechanism $(V'''_A$-$V'''_B)_A$, as well as a slight increase in the migration barriers upon increasing x. This conclusion is further supported by the correlations between the D^*_{La} versus the cation-vacancy concentration and the V'''_A-V'''_B concentration provided in Fig. S7 of Ref. [45], where the reduction of the D^*_{La} with increasing x at a given T and pO_2 mainly results from a decrease in cation-vacancy concentration and of the concentration of cation transport carriers.

Overall, based on the diffusion modeling results shown in Fig. 11, the apparent activation energies of D^*_{La} (slope of the diffusion coefficients versus $1/T$) in bulk LSM at $x = 0.0$–0.3 are predicted to have a weak dependence on the Sr'_A substitution level, whereas the predicted D^*_{La} exhibit 1–3 order differences in the magnitude. This finding is mainly attributed to influence of Sr substitution on the concentration of cation transport carriers.

VI. CONCLUSIONS

In this work, we perform a DFT-based modeling study to investigate the LSM defect energetics and migration barriers of the A-site and B-site cation diffusion pathways involving defect clusters. Guided by a bulk defect model which combines the DFT interaction energies of the defect clusters as well as the migration barriers of the active cation diffusion pathways, the predicted cation tracer diffusion coefficients obtained using a three-dimensional random-walk formalism are found to reasonably reproduce the experimental trends of the cation diffusivity versus T. We unveil a new active cation migration mechanism involving the V'''_A-V'''_B cluster as the transport carrier for the A-site cation transport, which exhibits a low migration barrier with values in the range 1.5–1.6 eV, which are in good agreement with the apparent activation energies of the experimental cation diffusivity measurements. The active B-site cation migration pathway for LSM also involves the V'''_A-V'''_B defect cluster, with a calculated barrier comparable to that of the active A-site migration mechanism. It is further identified that the Mn^x_A antisite migration *via* V'''_A exhibits a low barrier of 0.5 eV for the Mn diffusion in bulk LSM, which can lead to an alternative active Mn transport pathway through hopping of Mn^x_A-V'''_A on the A-site lattice, depending on the A/B cation ratio. Upon examination of the saddle configurations of the active cation transport pathways, it is revealed that the cation migration barriers can be significantly influenced by the defect cluster configurations. The diffusion barriers are found to exhibit correlations versus the ionic charges (due to electrostatic repulsion) and ionic radii (due to steric effects) among various migrating cations. The reduction of cation diffusivities in LSM with increasing Sr substitution level are further shown to be mainly due to decreases of the transport carrier concentration (i.e., cation vacancy and the defect clusters) and slight increase in the migration barriers. Our diffusion modeling results obtained based on the DFT energetics and migration barriers along with a bulk LSM defect model and a three-dimensional random-walk formalism provide both the mechanistic and energetic details to uncover the active cation diffusion pathways responsible for the experimentally measured cation diffusivities. This mechanistic information, together with the energetic results obtained, provide a foundation for rationalizing phenomena

associated with cation diffusion in bulk LSM at various synthetic compositions and under different operating conditions.

ACKNOWLEDGMENTS

This research is supported by the National Energy Technology Laboratory's ongoing research in the area of property assessment of diffused interface modeling in solid-oxide fuel cells. Y.-L. L. thanks the funding support from the National Energy Technology Laboratory Research Participation Program sponsored by the U.S. Department of Energy and administered by the Oak Ridge Institute for Science and Education. Y.-L. L. and Y. D. also thank Dr. Kirk Gerdes for his helpful comments on this work and careful readings of the manuscript. The views and opinions of authors expressed herein do not necessarily state or reflect those of the United States Government or any agency hereof.

[1] W. Shelton, G. Hackett, S. Vora, T. Shultz, and K. Gerdes, U.S. Department of Energy, National Energy Technology Laboratory Report No. DOE/NETL-341/112613, 2014.

[2] M. Backhaus-Ricoult, K. Adib, T. St. Clair, B. Luerssen, L. Gregoratti, and A. Barinov, *In-situ* study of operating SOFC LSM/YSZ cathodes under polarization by photoelectron microscopy, Solid State Ionics **179**, 891 (2008).

[3] H. Abernathy, H. O. Finklea, D. S. Mebane, X. Song, Y. Chen, and K. Gerdes, Examination of the mechanism for the reversible aging behavior at open circuit when changing the operating temperature of $(La_{0.8}Sr_{0.2})_{0.95}MnO_3$ electrodes, Solid State Ionics **272**, 144 (2015).

[4] K. Kleveland, M.-A. Einarsrud, C. R. Schmidt, S. Shamsili, S. Faaland, K. Wiik, and T. Grande, Reactions between strontium-substituted lanthanum manganite and yttria-stabilized zirconia: II, diffusion couples, J. Am. Ceram. Soc. **82**, 729 (1999).

[5] A. Chen, G. Bourne, K. Siebein, R. DeHoff, E. Wachsman, and K. Jones, Characterization of lanthanum zirconate formation at the *A*-site-deficient strontium-doped lanthanum manganite cathode/yttrium-stabilized zirconia electrolyte interface of solid oxide fuel cells, J. Am. Ceram. Soc. **91**, 2670 (2008).

[6] A.-K. Huber, M. Falk, M. Rohnke, B. Luerssen, M. Amati, L. Gregoratti, D. Hesse, and J. Janek, *In situ* study of activation and de-activation of LSM fuel cell cathodes—Electrochemistry and surface analysis of thin-film electrodes, J. Catal. **294**, 79 (2012).

[7] J. W. Stevenson, P. F. Hallman, T. R. Armstrong, and L. A. Chick, Sintering behavior of doped lanthanum and yttrium manganite, J. Am. Ceram. Soc. **78**, 507 (1995).

[8] S. P. Jiang and W. Wang, Sintering and grain growth of $(La, Sr)MnO_3$ electrodes of solid oxide fuel cells under polarization, Solid State Ionics **176**, 1185 (2005).

[9] D. L. Meixner and R. A. Cutler, Sintering and mechanical characteristics of lanthanum strontium manganite, Solid State Ionics **146**, 273 (2002).

[10] H. Yokokawa, Towards comprehensive description of stack durability/reliability behavior, Fuel Cells **15**, 652 (2015).

[11] J. Wolfenstine, K. C. Goretta, R. E. Cook, and J. L. Routbort, Use of diffusional creep to investigate mass transport in $(La, Sr)MnO_3$, Solid State Ionics **92**, 75 (1996).

[12] R. E. Cook, K. C. Goretta, J. Wolfenstine, P. Nash, and J. L. Routbort, High-temperature deformation and defect chemistry of $(La_{1-x}Sr_x)_{1-y}MnO_{3+\delta}$, Acta Mater. **47**, 2969 (1999).

[13] C.-C. T. Yang, W.-C. J. Wei, and A. Roosen, Reaction kinetics and mechanisms between $La_{0.65}Sr_{0.3}MnO_3$ and 8 mol% yttria-stabilized zirconia, J. Am. Ceram. Soc. **87**, 1110 (2004).

[14] J.-M. Hu, L. Liang, Y. Ji, L. Hong, K. Gerdes, and L.-Q. Chen, Interdiffusion across solid electrolyte-electrode interface, Appl. Phys. Lett. **104**, 213907 (2014).

[15] M. Palcut, K. Wiik, and T. Grande, Cation self-diffusion and nonstoichiometry of lanthanum manganite studied by diffusion couple measurements, J. Phys. Chem. C **111**, 813 (2007).

[16] S. Miyoshi and M. Martin, *B*-site cation diffusivity of Mn and Cr in perovskite-type $LaMnO_3$ with cation-deficit nonstoichiometry, Phys. Chem. Chem. Phys. **11**, 3063 (2009).

[17] M. Palcut, R. Knibbe, K. Wiik, and T. Grande, Cation interdiffusion between $LaMnO_3$ and $LaCoO_3$ materials, Solid State Ionics **202**, 6 (2011).

[18] S. P. Jiang, Development of lanthanum strontium manganite perovskite cathode materials of solid oxide fuel cells: A review, J. Mater. Sci. **43**, 6799 (2008).

[19] H. Yokokawa, N. Sakai, T. Kawada, and M. Dokiya, Thermodynamic analysis on interface between perovskite electrode and YSZ electrolyte, Solid State Ionics **40**, 398 (1990).

[20] R. A. De Souza, M. Saiful Islam, and E. Ivers-Tiffee, Formation and migration of cation defects in the perovskite oxide $LaMnO_3$, J. Mater. Chem. **9**, 1621 (1999).

[21] S. P. Harvey, R. A. De Souza, and M. Martin, Diffusion of La and Mn in $Ba_{0.5}Sr_{0.5}Co_{0.8}Fe_{0.2}O_{3-\delta}$ polycrystalline ceramics, Energy Environ. Sci. **5**, 5803 (2012).

[22] S. Miyoshi, J.-O. Hong, K. Yashiro, A. Kaimai, Y. Nigara, K. Kawamura, T. Kawada, and J. Mizusaki, Lattice creation and annihilation of $LaMnO_{3+\delta}$ caused by nonstoichiometry change, Solid State Ionics **154–155**, 257 (2002).

[23] J. Mizusaki *et al.*, Oxygen nonstoichiometry and defect equilibrium in the perovskite-type oxides $La_{1-x}Sr_xMnO_{3+d}$, Solid State Ionics **129**, 163 (2000).

[24] J. H. Kuo, H. U. Anderson, and D. M. Sparlin, Oxidation-reduction behavior of undoped and Sr-doped $LaMnO_3$ nonstoichiometry and defect structure, J. Solid State Chem. **83**, 52 (1989).

[25] F. W. Poulsen, Defect chemistry modelling of oxygen-stoichiometry, vacancy concentrations, and conductivity of $(La_{1-x}Sr_x)_yMnO_{3+/-\delta}$, Solid State Ionics **129**, 145 (2000).

[26] D. S. Mebane, Y. J. Liu, and M. L. Liu, Refinement of the bulk defect model for $La_xSr_{1-x}MnO_{3+/-\delta}$, Solid State Ionics **178**, 1950 (2008).

[27] Y.-L. Lee and D. Morgan, *Ab initio* and empirical defect modeling of $LaMnO_{3\pm\delta}$ for solid oxide fuel cell cathodes, Phys. Chem. Chem. Phys. **14**, 290 (2012).

[28] M. Kilo, M. A. Taylor, C. Argirusis, G. Borchardt, R. A. Jackson, O. Schulz, M. Martin, and M. Weller, Modeling of cation diffusion in oxygen ion conductors using molecular dynamics, Solid State Ionics **175**, 823 (2004).

[29] B. Puchala, Y.-L. Lee, and D. Morgan, *A*-site diffusion in $La_{1-x}Sr_xMnO_3$: *Ab initio* and kinetic Monte Carlo calculations, J. Electrochem. Soc. **160**, F877 (2013).

[30] R. A. De Souza and J. Maier, A computational study of cation defects in $LaGaO_3$, Phys. Chem. Chem. Phys. **5**, 740 (2003).

[31] O. Schulz, M. Martin, C. Argirusis, and G. Borchardt, Cation tracer diffusion of $^{138}La^{84}Sr$ and ^{25}Mg in polycrystalline $La_{0.9}Sr_{0.1}Ga_{0.9}Mg_{0.1}O_{2.9}$, Phys. Chem. Chem. Phys. **5**, 2308 (2003).

[32] M. Palcut, J. S. Christensen, K. Wiik, and T. Grande, Impurity diffusion of ^{141}Pr in $LaMnO_3LaCoO_3$ and $LaFeO_3$ materials, Phys. Chem. Chem. Phys. **10**, 6544 (2008).

[33] G. Kresse and J. Hafner, *Ab initio* molecular dynamics for liquid metals, Phys. Rev. B **47**, 558 (1993).

[34] G. Kresse and J. Furthmuller, Efficient iterative schemes for *ab initio* total-energy calculations using a plane-wave basis set, Phys. Rev. B **54**, 11169 (1996).

[35] G. Kresse and D. Joubert, From ultrasoft pseudopotentials to the projector augmented-wave method, Phys. Rev. B **59**, 1758 (1999).

[36] J. P. Perdew, K. Burke, and M. Ernzerhof, Generalized Gradient Approximation Made Simple, Phys. Rev. Lett. **77**, 3865 (1996).

[37] V. I. Anisimov, J. Zaanen, and O. K. Andersen, Band theory and Mott insulators—Hubbard U instead of Stoner I, Phys. Rev. B **44**, 943 (1991).

[38] S. L. Dudarev, G. A. Botton, S. Y. Savrasov, C. J. Humphreys, and A. P. Sutton, Electron-energy-loss spectra and the structural stability of nickel oxide: An LSDA + U study, Phys. Rev. B **57**, 1505 (1998).

[39] L. Wang, T. Maxisch, and G. Ceder, Oxidation energies of transition metal oxides within the GGA + U framework, Phys. Rev. B **73**, 195107 (2006).

[40] Y.-L. Lee, J. Kleis, J. Rossmeisl, and D. Morgan, *Ab initio* energetics of $LaBO_3(001)$ (B = Mn, Fe, Co, and Ni) for solid oxide fuel cell cathodes, Phys. Rev. B **80**, 224101 (2009).

[41] H. J. Monkhorst and J. D. Pack, Special points for Brillouin-zone integrations, Phys. Rev. B **13**, 5188 (1976).

[42] J. F. Mitchell, D. N. Argyriou, C. D. Potter, D. G. Hinks, J. D. Jorgensen, and S. D. Bader, Structural phase diagram of $La_{1-x}Sr_xMnO_{3+\delta}$: Relationship to magnetic and transport properties, Phys. Rev. B **54**, 6172 (1996).

[43] G. Henkelman and H. Jónsson, Improved tangent estimate in the nudged elastic band method for finding minimum energy paths and saddle points, J. Chem. Phys. **113**, 9978 (2000).

[44] F. A. Kröger and H. J. Vink, in *Solid State Physics*, edited by S. Frederick and T. David (Academic Press, New York, 1956), p. 307.

[45] See Supplemental Material at http://link.aps.org/supplemental/10.1103/PhysRevApplied.8.044001 for the bulk defect and diffusion modeling approaches and results, the definition of the Kröger-Vink notation of the symbols, summary of the calculated migration barriers, configurations of the defect interaction calculations, Sr ordering, migration pathways in the simulated supercells, and potential energy profiles of the cation migration pathways at different Sr and magnetic ordering.

[46] M. Pavone, A. B. Muñoz-García, A. M. Ritzmann, and E. A. Carter, First-principles study of lanthanum strontium manganite: Insights into electronic structure and oxygen vacancy formation, J. Phys. Chem. C **118**, 13346 (2014).

[47] J. He, M.-X. Chen, X.-Q. Chen, and C. Franchini, Structural transitions and transport-half-metallic ferromagnetism in $LaMnO_3$ at elevated pressure, Phys. Rev. B **85**, 195135 (2012).

[48] G. Makov and M. C. Payne, Periodic boundary-conditions in *ab initio* calculations, Phys. Rev. B **51**, 4014 (1995).

[49] P. Mondal, D. Bhattacharya, P. Choudhury, and P. Mandal, Dielectric anomaly at T_N in $LaMnO_3$ as a signature of coupling between spin and orbital degrees of freedom, Phys. Rev. B **76**, 172403 (2007).

[50] K. Kamata, T. Nakajima, T. Hayashi, and T. Nakamura, Nonstoichiometric behavior and phase stability of rare earth manganites at 1200 °C: (1). $LaMnO_3$, Mater. Res. Bull. **13**, 49 (1978).

[51] H. Mehrer, *Diffusion in Solids: Fundamentals, Methods, Materials, Diffusion-Controlled Processes* (Springer-Verlag, Berlin, 2007).

[52] I. V. Belova, G. E. Murch, D. Samuelis, and M. Martin, Collective and tracer diffusion via a defect cluster in LSGM, Defect Diffus. Forum **263**, 81 (2007).

[53] G. Brouwer, A general asymptotic solution of reaction equations common in solid-state chemistry, Philips Res. Rep. **9**, 366 (1954).

[54] K. Nakamura, The defect chemistry of $La_{1-\Delta}MnO_{3+\delta}$, J. Solid State Chem. **173**, 299 (2003).

[55] A. N. Grundy, B. Hallstedt, and L. J. Gauckler, $La_{1-x}Mn_{1-y}O_{3-z}$ perovskites modelled with and without antisite defects using the CALPHAD approach, Solid State Ionics **173**, 17 (2004).

[56] P. Dalach, D. E. Ellis, and A. van de Walle, First-principles thermodynamic modeling of lanthanum chromate perovskites, Phys. Rev. B **85**, 014108 (2012).

[57] A. V. Berenov, J. L. MacManus-Driscoll, and J. A. Kilner, Oxygen tracer diffusion in undoped lanthanum manganites, Solid State Ionics **122**, 41 (1999).

[58] K. Momma and F. Izumi, VESTA 3 for three-dimensional visualization of crystal, volumetric and morphology data, J. Appl. Crystallogr. **44**, 1272 (2011).

[59] Y. Dong, L. Qi, J. Li, and I. W. Chen, A computational study of yttria-stabilized zirconia: II. Cation diffusion, Acta Mater. **126**, 438 (2017).

[60] L. Pauling, The principles determining the structure of complex ionic crystals, J. Am. Chem. Soc. **51**, 1010 (1929).

[61] H. Mizoguchi, H. W. Eng, and P. M. Woodward, Probing the electronic structures of ternary perovskite and pyrochlore oxides containing Sn^{4+} or Sb^{5+}, Inorg. Chem. **43**, 1667 (2004).

[62] R. Shannon, Revised effective ionic radii and systematic studies of interatomic distances in halides and chalcogenides, Acta Crystallogr. Sect. A **32**, 751 (1976).

[63] M. Wołcyrz, R. Horyń, F. Bourée, and E. Bukowska, Structural defects in $LaMnO_3$ phase studied by neutron diffraction, J. Alloys Compd. **353**, 170 (2003).

[64] R. Horyń, A. Sikora, and E. Bukowska, Polymorphic forms and defect structure formation within homogeneity domain of $LaMnO_3$ phase, J. Alloys Compd. **353**, 153 (2003).

[65] L. Malavasi, C. Ritter, M. Cristina Mozzati, C. Tealdi, M. Saiful Islam, C. Bruno Azzoni, and G. Flor, Effects of cation vacancy distribution in doped $LaMnO_{3+\delta}$ perovskites, J. Solid State Chem. **178**, 2042 (2005).